PHYSICAL REVIEW FLUIDS **7**, 124603 (2022)

Investigation of reaction-induced subgrid scalar mixing in LES/FDF simulations of turbulent premixed flames

Xiao Wang,[1] Jieli Wei,[1] Xingyu Su,[2,3] Hua Zhou,[1,*] and Zhuyin Ren[1,3]
[1]*Institute for Aero Engine, Tsinghua University, Beijing 100084, China*
[2]*Department of Energy and Power Engineering, Tsinghua University, Beijing 100084, China*
[3]*Center for Combustion Energy, Tsinghua University, Beijing 100084, China*

(Received 30 June 2022; accepted 23 November 2022; published 14 December 2022)

Large eddy simulation (LES) combined with filtered density function (FDF), i.e., LES/FDF, is an effective approach for high-fidelity simulation of turbulent flames. In this work, LES/FDF simulations are performed for the turbulent piloted premixed methane-air flame F3 to investigate the impact of reaction-induced subgrid scalar mixing on the predicted flame characteristics. The effects of mixing formulation on flame characteristics, as well as the performance of the classic constant mechanical-to-scalar mixing timescale model, are investigated, illustrating that reaction-induced scalar gradient plays an important role in determining the species mixing frequency. A new closure of scalar mixing timescale (hybrid-DD) is proposed to account for the reaction-induced differential mixing among species. The model adaptively adjusts the relative contribution from turbulence and reaction and requires no *ad hoc* model parameters to be specified manually. It is found that the hybrid-DD model yields a reasonable prediction of the overall combustion process of the flame F3, notably better than the conventional constant mechanical-to-scalar mixing timescale model with the nonoptimal model constant. The predicted scalar mixing frequency by the hybrid-DD model is found to exhibit differences among species, resulting in more abundant thermochemical states. Considering that all the components of the hybrid-DD model are readily available in the transported FDF method, the model is a promising candidate to be employed in LES/FDF simulations of turbulent premixed flames.

DOI: 10.1103/PhysRevFluids.7.124603

I. INTRODUCTION

Turbulent premixed combustion is a technology commonly applied in many modern combustion devices for high combustion efficiency and low pollutant emissions. A fundamental understanding of complicated flame dynamics and turbulence-chemistry interaction in turbulent premixed combustion is essential for reliable combustor design. The transported probability density function (TPDF) method [1–5], one of the advanced approaches for turbulent flame simulation, provides an elegant solution to the closure of the mean chemical source term without any approximation and is capable of reliable prediction for turbulent flames such as the near-limit flame [6] and the dilute spray flame [7]. Despite some reported success in turbulent non-premixed combustion simulations [8–19], the simulation for turbulent premixed combustion when applying TPDF methods remains challenging. In particular, the conditional molecular diffusion term is arguably more difficult to model since the local gradients of chemical species are driven principally by reaction-diffusion interaction for premixed flames at least when the Karlovitz number is small.

Many efforts have been made to model the conditional molecular diffusion [20–28]. Considering the simplicity of implementation and the guarantee of realizability, the three widely applied

---

[*] Corresponding author: zhouhua@mail.tsinghua.edu.cn

micromixing models are the interaction by exchange with the mean (IEM) or linear mean-square estimation model [20,21], the modified Curl's (MC) model [22,23], and the Euclidean minimum spanning tree (EMST) model [24]. Recently, some new mixing models such as the multiple mapping conditioning model [25,26] and shadow-position conditioning [27,28] have been developed as well. While the mixing models describe the manner in which mixing occurs, the specification of mixing timescale is required to describe how fast the scalar PDF changes. Studies based on a direct numerical simulation (DNS) dataset illustrate that the scalar mixing timescale is critical for a TPDF simulation of turbulent premixed combustion [29]. The most widely applied mixing timescale model is the constant mechanical-to-scalar mixing timescale model. The model essentially assumes that the scalar mixing timescale is proportional to the turbulence timescale by a constant. However, it has been well recognized that the assumption of constant mechanical-to-scalar timescale ratio is questionable for reactive scalars, especially in turbulent premixed flames where both turbulence and chemical reactions play important roles in varying the species gradients [30], and thus both factors have significant influence on the mixing timescale of species [31–33].

Accounting for the reaction-induced scalar mixing has been a feasible way to improve the accuracy of TPDF simulation for the turbulent premixed flames and has been attracting a great deal of attention [34–42]. To circumvent the difficulty of modeling the scalar mixing in turbulent premixed flame, Pope and Anand [34] proposed a closure by mapping the mixture state to a 1D freely propagating premixed flame. However, the intrinsic assumption of embedded laminar flamelets limits the applicability of such closure. Later, Kolla *et al.* [35] and Lindstedt *et al.* [36,37] separately proposed algebraic models for the scalar dissipation rate of chemical species in turbulent premixed flames. These models account for dilatation, turbulence-scalar interaction, chemical reactions, and scalar dissipation, but are limited to turbulent premixed flames with high Damköhler numbers. To capture the transition to more intense turbulent combustion regimes, Stöllinger and Heinz [38] and Kuron *et al.* [39] proposed their scalar mixing timescale models based on the idea of linear blending by Mura *et al.* [40], i.e., linearly blends a mixing timescale model for the flamelet regime and another model for the broken-reaction-zones regime. These are valuable efforts made to incorporate the reaction-induced mixing for reactive scalars in the Reynolds-averaged (RANS) framework. The modeling of reactive scalar mixing in the context of large eddy simulation (LES) is arguably more difficult, considering that the subgrid scalar mixing becomes dependent on the filter width, requiring the model to be locally adaptive to the LES filter. Tirunagari and Pope [41] and Wang *et al.* [42] separately proposed their mixing timescale models for reactive scalars in turbulent premixed flames, and both employed the filter width (Δ), the laminar flame thickness (δ_L), and the subgrid turbulence frequency (Ω^t) to formulate the models. The former one by Tirunagari and Pope scales as $(\Delta/\delta_L)\Omega^t$, while the latter one by Wang scales as $(\Delta/\delta_L)^2\Omega^t$. These models have been demonstrated to improve the prediction of the macroscopic properties of turbulent premixed flames, e.g., the overall combustion progress, turbulent flame speed, and mean temperature.

Despite being valuable, the major assumption in the above studies is that the mixing characteristics of all composition variables can be represented by that of one reactive scalar, mostly taken to be progress variable. However, it is known that the mixing timescales of species depend on the gradients caused by chemical reaction in turbulent premixed flames. Therefore, chemical species feature their own characteristic length scales and timescales, resulting in different controlling processes for the mixing of species, and thus, the difference in mixing timescales among species. It has also been proved in the DNS studies [43,44] that the mixing timescales of species are very different from each other. The recent study by Zhou *et al.* [45,46] indicates that taking account for differential mixing timescales in TPDF simulations yields notable improvement in the prediction of the overall combustion process.

Nevertheless, there are few studies considering reaction-induced differential mixing in TPDF simulations. On the one hand, most of the widely applied micromixing models, e.g., IEM, MC, and EMST, cannot incorporate differential mixing timescales while ensuring the realizability condition of the species mass fraction summing to unity. On the other hand, mixing timescale models that account for reaction-induced differential mixing are still in their infancy. A model for the dissipation rate of each individual species was once proposed by Richardson *et al.* [44] based on the reference laminar flame. The model employs the species gradients obtained from laminar flames to estimate the relative magnitude of the species dissipation rates in turbulent flames, thus the model is expected to be valid in the flamelet regime, but not in the thin-reaction-zones or broken-reaction-zones regime. To cover the full combustion regime of turbulent premixed flames, Zhou *et al.* [47] proposed a mixing timescale model for each individual species by extending Kuron's model [39]. However, none of these models have been employed in *a posteriori* TPDF simulations. More importantly, these models were originally proposed for the RANS framework. Modeling the reaction-induced differential mixing in the context of LES warrants further investigation.

The primary objective of this work is to evaluate the potential benefit of incorporating reaction-induced differential mixing in LES simulations of turbulent premixed flames using the TPDF method, i.e., LES/filtered density function (FDF). This is done by making head-to-head comparisons between different modeling approaches for scalar mixing timescales in LES/FDF simulations. To achieve this, a new closure of scalar mixing timescale (hybrid-DD) is proposed to account for the reaction-induced differential mixing among species, and the recently proposed MC-DD models by Yang *et al.* [48] are applied to incorporate differential mixing timescales while ensuring the realizability condition. The remainder of this paper is organized as follows: In Sec. II, the LES/FDF method, the newly proposed scalar mixing timescale model, and the case settings are presented. In Sec. III, the assessment of different micromixing models and mixing timescale models are presented, and the effect of reaction-induced differential mixing is discussed. Conclusions are presented in Sec. IV.

II. METHODOLOGY

A. LES/FDF method

The joint composition FDF method is employed for LES modeling to handle turbulence-chemistry interaction at the subgrid scale. The joint composition FDF is defined as $f(\boldsymbol{\psi};\boldsymbol{x},t)$ with $\boldsymbol{\psi}$ being the phase variable corresponding to composition vector $\boldsymbol{\phi} = (Y_1, Y_2, \ldots, Y_N, h_s)$, and the governing equation for $f(\boldsymbol{\psi};\boldsymbol{x},t)$ yields

$$\begin{aligned}\frac{\partial \rho f}{\partial t} &+ \frac{\partial}{\partial x_i}(\tilde{U}_i \rho f) + \frac{\partial}{\partial \psi_k}(S_k \rho f)\\ &= -\frac{\partial}{\partial x_i}(\langle U_i''|\boldsymbol{\psi}\rangle \cdot \rho f) + \frac{\partial}{\partial \psi_k}\left(\frac{\partial \tilde{J}_{i,k}}{\partial x_i} f\right) + \frac{\partial}{\partial \psi_k}\left(\left\langle \frac{1}{\rho}\frac{\partial J''_{i,k}}{\partial x_i}\middle|\boldsymbol{\psi}\right\rangle \cdot \rho f\right),\end{aligned} \tag{1}$$

where $\tilde{U}_i$ and U_i'' are the ith component of the Favre-averaged mean and fluctuating velocity; S_k is the source term for the kth composition; and $J_{i,k}$ is the ith component of the transported flux of the kth composition due to molecular diffusion. The second term on the right-hand side of Eq. (1) represents the transported flux due to molecular diffusion at the resolved scale in LES, while the last term is the conditional diffusion flux at the subgrid scale, which is one of the most important terms to be modeled in a LES/FDF simulation.

The solution to the governing equation of $f(\boldsymbol{\psi};\boldsymbol{x},t)$ is obtained via a two-way coupled scheme between a finite volume solver and a Monte Carlo particle solver [13,49,50]. The finite volume LES solver solves the filtered continuity and momentum transport equations in a cylindrical coordinate, with a second-order conservative scheme being applied for discretization, while continuity is enforced by solving the pressure Poisson equation. A set of stochastic differential equations of the notional Lagrangian particles are shown, governing the evolution in physical and composition space:

$$d\boldsymbol{x}^* = [\tilde{\boldsymbol{U}} + \nabla(\tilde{\Gamma}_t \bar{\rho})/\bar{\rho}]^* dt + [2(\tilde{\Gamma} + \tilde{\Gamma}_t)^*]^{1/2} d\boldsymbol{W}^*, \tag{2}$$

$$d\boldsymbol{\phi}^*(t) = \boldsymbol{M}^* dt + \boldsymbol{S}(\boldsymbol{\phi}^*) dt, \tag{3}$$

where $\boldsymbol{x}^*$ and $\boldsymbol{\phi}^*$ are the spatial location and composition of an individual particle, respectively, and the superscript "*" denotes a value of the filtered LES field evaluated at the particle's location. The bar ($\bar{}$) and tilde ($\sim$) represent spatial filtering and density-weighted spatial filtering, respectively. Therefore, $\tilde{\boldsymbol{U}}$ is the Favre-averaged mean velocity, $\bar{\rho}$ is filtered density, $\tilde{\Gamma}$ and $\tilde{\Gamma}_t$ represent the filtered molecular diffusivity and turbulent diffusivity. $d\boldsymbol{W}^*$ is an independent Wiener increment, $\boldsymbol{S}(\boldsymbol{\phi}^*)$ is the reaction rate, representing the chemical reaction source term, and $\boldsymbol{M}^*$ represents the rate of change in composition due to micromixing. In terms of the coupling between the two solvers, the LES solver provides the filtered velocity, molecular, and turbulent diffusivity to the particle solver, while the particle solver provides the filtered temperature and the source term of the specific volume (reciprocal of the filtered density, $1/\overline{\rho}$) to the LES solver. Note that the filtered density computed from the computational particles contains considerable random noise due to the nature of the Monte Carlo approach; a transport equation for the specific volume is solved to obtain a smoothed filtered density consistent with the Monte Carlo particles.

The modeling of $\boldsymbol{M}^*$, i.e., micromixing, is the key to the accuracy of LES/FDF simulations and is essentially the focus of the study. A micromixing model in general involves two ingredients: the mixing format and the scalar mixing timescale. Three widely used mixing formats, i.e., IEM [20,21], MC [22,23], and EMST [24] models are employed as the baseline setting. In addition, the recently proposed MC-DD model [48] is employed to account for differential mixing.

The MC-DD model allows the mixing timescale for each individual species to be specified explicitly to investigate the effects of differential mixing. In the MC-DD model, the composition of particle p among the pair (p, q) evolves according to a mass-based formulation ensuring the realizability condition of the species mass fraction summing to unity:

$$\begin{aligned} m_i^{(p)} &= (1-\alpha\theta_i)\, m_{i,0}^{(p)} + \alpha\theta_i\, m_0^{(p)} \tilde{Y}_i^{(p,q)}, \qquad i = 1, \dots, N_s \\ \tilde{Y}_i^{(p,q)} &= \frac{m_{i,0}^{(p)} + m_{i,0}^{(q)}}{m_0^{(p)} + m_0^{(q)}}, \end{aligned} \tag{4}$$

$$\begin{aligned} H_s^{(p)} &= \left(1-\alpha\theta_{h_s}\right) H_{s,0}^{(p)} + \alpha\theta_{h_s} m_0^{(p)} \tilde{h}_s^{(p,\,q)}, \\ \tilde{h}_s^{(p,\,q)} &= \frac{H_{s,0}^{(p)} + H_{s,0}^{(q)}}{m_0^{(p)} + m_0^{(q)}}, \end{aligned} \tag{5}$$

where $m_i^{(p)}$ and $H_s^{(p)}$ represent the mass of species i and the sensible enthalpy contained in particle p, respectively. The subscript 0 denotes the quantities before mixing and α is a random number uniformly distributed between 0 and 1. In order to produce the exponential decay of the species variance with the specified decay rate, θ_i and θ_{h_s} are the specified decay factor for each species and enthalpy, respectively. For example, when $\theta_i = 0$, the mixing frequency for the ith composition is zero, i.e., no mixing; when $\theta_i = 1$, the ith composition has the maximum mixing frequency among all the compositions defined as $\Omega_{\max} = \max\{\Omega_1, \Omega_2, \dots, \Omega_{N_s+1}\}$. To accomplish mixing at an arbitrary frequency with $\Omega_i < \Omega_{\max}$, the differential diffusion is accounted for by specifying different decay rates for different individual species as

$$\theta_i = \frac{3-\sqrt{9-8\omega_i}}{2}, \quad i = 1, \dots, N_s+1, \tag{6}$$

where the relative decay rate is $\omega_i = \Omega_i/\Omega_{\max}$, and Ω_i is the mixing frequency of the composition i, which will be computed in the next section. Note that if a single representative mixing frequency is used for all the species, MC-DD will recover the conventional MC model.

B. Scalar mixing timescale model

Each mixing formulation is coupled with a specification of the scalar mixing timescale, which is affected by turbulence strain and chemical reaction through the steepening of species gradients [30]

$$\frac{D}{Dt}\left(\frac{\partial Y_i}{\partial x_j}\right) = \frac{1}{\rho}\nabla\cdot\left[\rho\Gamma\nabla\left(\frac{\partial Y_i}{\partial x_j}\right)\right] - \frac{\partial U_k}{\partial x_j}\frac{\partial Y_i}{\partial x_k} + \frac{\partial S_i}{\partial Y_k}\frac{\partial Y_k}{\partial x_j}, \tag{7}$$

where the three terms on the right-hand side represent diffusion, straining, and reaction, respectively. This indicates that the chemical reaction would have great influence on species gradients, especially when the Damköhler number (Da) is large. As a result, the species mixing timescale of any species would be affected strongly by the flame structure, and differences in the species gradients would be induced by reaction, in turn resulting in the significant difference in mixing frequency among species. The mixing frequency of the ith species, Ω_i (reciprocal of the corresponding scalar mixing timescale), determines the decay rate of the subfilter scale scalar variance due to molecular diffusion. Following its definition, Ω_i is defined as

$$\Omega_i = \tilde{\chi}_i / \widetilde{Y_i''^2}, \tag{8}$$

where $\tilde{\chi}_i = 2\Gamma_i \widetilde{\nabla Y_i'' \cdot \nabla Y_i''}$ is the Favre-averaged scalar dissipation rate, Γ_i represents the species molecular diffusivity, and $\widetilde{Y_i''^2}$ is the Favre-averaged scalar variance.

For the classic constant mechanical-to-scalar timescale model [51,52], the mixing frequency of all species is assumed to be equal to the subgrid turbulence frequency; the mixing frequency of the ith species therefore yields

$$\Omega_i^{\mathrm{const}} = C_M \frac{\Gamma + \Gamma_t}{\Delta^2}, \tag{9}$$

where Γ and Γ_t are the thermal diffusivity and turbulent diffusivity, respectively, and Δ is the filter length scale. As described in Sec. I, the mechanical-to-scalar timescale model constant C_M is critical to the simulation, of which the optimal value has a wide variation even for flames in the same configuration. Considering that C_M is *ad hoc* and needs to be specified manually, the constant mechanical timescale model does not appear to be viable for turbulent premixed flames in general.

A dynamic closure [52] has been proposed to circumvent the difficulty of specifying the case-dependent model constant C_M manually. The closure is based on the dynamic modeling of subgrid variance ($\bar{\rho}\widetilde{\xi''^2}$) and scalar dissipation rate ($\bar{\rho}\tilde{\chi}_\xi$) of a passive scalar ξ. Therefore, it is important to appreciate that the closure only aims at modeling passive scalar mixing and could be problematic when applied to reactive scalar mixing. The mixing frequency is computed as

$$\Omega_i^{\mathrm{Dyn}} = C_M^{\mathrm{Dyn}} \frac{\Gamma_t}{\Delta^2}, \tag{10}$$

where C_M^{Dyn} is computed dynamically via an algebraic scaling law; readers are referred to Ref. [53] for details. Note that the selection of the characteristic passive scalar depends on the specific problem. In this work, the central jet mixture fraction is chosen to construct mixing frequency since the mixing between the central and pilot (coflow) stream affects the combustion process.

To account for the reaction-induced scalar gradients, Kuron *et al.* [39] proposed a hybrid mixing timescale for RANS/PDF simulations of turbulent premixed flames. Later, Yang *et al.* [53] extended this model for the application in LES/FDF simulations. The hybrid mixing timescale model assumes that the mixing timescale of all species can be reasonably represented by that of the reaction progress variable, and the mixing timescale of progress variable has a linear blending formulation

$$\Omega_i^{\mathrm{Hyb}} = (1 - \eta)\Omega^t + \eta \Omega_c^f, \tag{11}$$

where η is the segregation factor characterizing the relative contribution of the turbulence-induced mixing (Ω^t) and the reaction-induced mixing for progress variable (Ω_c^f). Specifically, η is defined as the normalized local variance of the progress variable c, both bounded between 0 and 1:

$$\eta = \left[\overline{\overline{\widetilde{c^2}}} - \left(\overline{\overline{\tilde{c}}}\right)^2\right] / \overline{\overline{\tilde{c}}}\left(1 - \overline{\overline{\tilde{c}}}\right), \tag{12}$$

where the double overbar represents the spatial averaging over the statistical homogeneous direction, i.e., circumferential direction for the free shear jet configuration, and tilde represents the Favre averaging. The progress variable c is defined as the mass of carbon element in CO_2 and CO over

TABLE I. The features of different mixing timescale models.

Mixing timescale model	Dynamic closure	Reaction-induced mixing	Differential mixing
Constant model ($\Omega_i^{\mathrm{const}}$)	×	×	×
Dynamic model (Ω_i^{Dyn})	√	×	×
Hybrid model (Ω_i^{Hyb})	√	√	×
Hybrid-DD model ($\Omega_i^{\mathrm{Hyb-DD}}$)	√	√	√

the total mass of carbon element of the mixture in this work. When the local Da is much smaller than 1, η approaches 0, and scalar mixing is governed by turbulent mixing. Conversely, when local Da $\gg$ 1, η approaches 1, and scalar mixing is governed by reaction-induced mixing.

The turbulence-induced mixing frequency Ω^t is modeled by the dynamic model in Eq. (10), and the reaction-induced mixing frequency Ω_c^f is reconstructed from laminar reference flames, which is formulated as

$$\Omega_c^f = \widetilde{\chi}_f^c/\widetilde{c''^2} = \int_0^1 \overline{\chi_c|\zeta}\,\widetilde{f}_c(\zeta)d\zeta\ /\widetilde{c''^2}, \tag{13}$$

where $\widetilde{\chi}_f^c$ is the Favre-averaged scalar dissipation rate obtained from the reference laminar flame, computed by the conditional filtered scalar dissipation rate $\overline{\chi_c|\zeta}$ and the density-weighted filtered density function $\overline{f_c}(\zeta)$ of the progress variable. The modeling of Ω_f takes advantage of LES/FDF methods in which $\overline{f_c}(\zeta)$ is a part of the solution for individual particles. Thus, the hybrid mixing frequency adaptively changes depending on the filter size and state of combustion.

To account for the difference in species mixing timescale due to the difference in species gradients induced by chemical reaction, Zhou *et al.* [47] extended Kuron's model and proposed a mixing timescale model for each individual species for RANS/PDF simulations. In this work, Zhou's model was extended to LES/FDF simulations, which yields

$$\Omega_i^{\mathrm{Hyb-DD}} = (1-\eta)\Omega^t + \eta\Omega_i^f. \tag{14}$$

Here Ω^t is modeled by Eq. (10) and Ω_i^f represents the reaction-induced mixing frequencies of the ith species, which yields

$$\tilde{\chi}_i^f = \int_0^1 \langle 2D_i\nabla Y_i\cdot\nabla Y_i|c=\zeta\rangle\widetilde{f}_c(\zeta)d\zeta = \int_0^1 (2D_i\nabla Y_i\cdot\nabla Y_i)^{\mathrm{lam}}\tilde{f}_c(\zeta)d\zeta, \tag{15}$$

where D_i is the molecular diffusivity of the ith species. Thus, the model described by Eq. (14) accounts for the effects of both turbulence strain and chemical reaction on the mixing timescale of each individual species.

Table I presents the features of three mixing timescale models, i.e., $\Omega_i^{\mathrm{const}}$ by Eq. (9), Ω_i^{Dyn} by Eq. (10), Ω_i^{Hyb} by Eq. (11), and $\Omega_i^{\mathrm{Hyb-DD}}$ by Eq. (14). As shown, $\Omega_i^{\mathrm{const}}$ ignores both the reaction-induced mixing and the differential mixing and needs to be adjusted manually; Ω_i^{Dyn} provides a dynamic closure but ignores the reaction-induced mixing and differential mixing; Ω_i^{Hyb} provides a dynamic closure and accounts for the reaction-induced mixing, but ignores the differential mixing; $\Omega_i^{\mathrm{Hyb-DD}}$ features all three aspects.

C. Flame configuration and simulation settings

The premixed turbulent flame investigated in this work is produced by a piloted Bunsen burner, experimentally studied by Chen *et al.* [54], which gives a stationary mean flow field and is easier for numerical simulations to study the interaction between flame propagation and turbulence structure. The burner consists of a nozzle for main stream with diameter $D = 12$ mm, and a large pilot flame to stabilize the turbulent main jet flame. The pilot stream is generated from a perforated plate (1175 holes of 1 mm diameter each) around the central nozzle. Three stoichiometric turbulent Bunsen flames (F1, F2, and F3) at different exit velocities were investigated by Chen *et al.* [54]. In this work, the F3 flame is chosen due to its large Damköhler number (Da). The large Da indicates the strong reaction-induced species gradient and differential mixing; therefore, the target flame serves the purpose of investigating the benefit of incorporating reaction-induced differential mixing in TPDF simulations of turbulent premixed flames. For the flame F3, the mean nozzle exit velocity is $U_0 = 30\ \mathrm{m/s}$ and the corresponding Reynolds number $\mathrm{Re} = 24\,200$. The estimated Karlovitz number 3.4 by Stöllinger and Heinz [38] indicates that the F3 flame falls into the thin-reaction zones and is close to the borderline of the corrugated flamelet regime in the modified turbulent premixed combustion diagram of Peters [55]. In this regime, turbulence is able to thicken the flame preheat zone but not the reaction zone.

The LES/FDF simulation domain is a three-dimensional axisymmetric cylinder, which extends to $40D$ downstream in the axial direction and $20D$ in the radial direction. The domain is divided into $168 \times 112 \times 48$ (axial, radial, and azimuthal, respectively) structured grid cells, and the grid is stretched to the boundary to ensure the fine resolution in the near-field region. The characteristic grid width, i.e., $\Delta = (\Delta x \times \Delta r \times r\Delta\theta)^{1/3}$ ranges from 0.12 to 1.55 mm in the main flame zone defined as $r/D \leqslant 2$ where the mixing and combustion of the central jet mixture mostly occur. Considering that the thermal laminar flame thickness (δ_L) of the stoichiometric methane-air mixture is around 0.5 mm, Δ/δ_L ranges from 0.24 to 3.10 in the main flame zone, indicating a modest grid resolution in terms of resolving the flame structure. The simulation runs for around six flow-through time to reach the statistical stationary state, then the time average is taken for around three flow-through time for statistics. For the inlet velocity, the jet inflow boundary is generated from a separate LES simulation of a fully developed pipe flow with the same Re as the central jet flow. A uniform inflow velocity profile is applied to the pilot and coflow streams according to the work by Wang *et al.* [42]. The convective boundary condition is prescribed at the lateral and outflow boundaries [56]. As for the inlet composition, the coflow stream consists of ambient air, the jet stream consists of a stoichiometric methane-air mixture, and the pilot stream is comprised of products by a stochiometric methane-air mixture combustion. Considering the 20% heat loss to the burner, the temperature of the pilot is specified to be 1785 K [37,42] while the temperature of the jet and coflow is 300 K.

The Vreman algebraic subgrid model [57] is used to compute the subgrid turbulent viscosity, with the Smagorinsky constant taken to be 0.1. The subgrid turbulent diffusivity is computed from the subgrid turbulent viscosity using a turbulent Schmidt number (Sc_t) of 0.4 [58]. The sensitivity of the Schmidt number is investigated in Ref. [6], indicating that the difference due to the variation of Sc_t is very minor. The molecular diffusivity is computed using the unity Lewis number assumption. The employed chemical reaction is an augmented reduced mechanism of GRI1.2, i.e., ARM1 mechanism [59] consisting of 16 species and 12-step reactions. The composition change due to chemical reactions is treated by the *in situ* adaptive tabulation (ISAT) method developed by Pope [60], with the ISAT error tolerance being set to 5×10^{-5}. The nominal number of particles per cell is 20, which has been demonstrated to be sufficient for numerical accuracy [47]. The species mixing frequency is handled by the mixing timescale models presented in the previous section, i.e., $\Omega_i^{\mathrm{const}}$ by Eq. (9), Ω_i^{Dyn} by Eq. (10), Ω_i^{Hyb} by Eq. (11), and $\Omega_i^{\mathrm{Hyb-DD}}$ by Eq. (14). The mixing formulation is taken to be IEM, MC, EMST, IEM-DD, or MC-DD.

III. RESULTS AND DISCUSSIONS

A. Effects of mixing models on flame characteristics

By comparing the LES/FDF simulation results with three different micromixing models, i.e., IEM, MC, and EMST, a qualitative examination of the flame shapes is first performed to illustrate the impact of the micromixing model on the target flame. The constant mechanical timescale model is applied with the model constant C_M being 2 and 12 for comparison. Figure 1 shows the contour

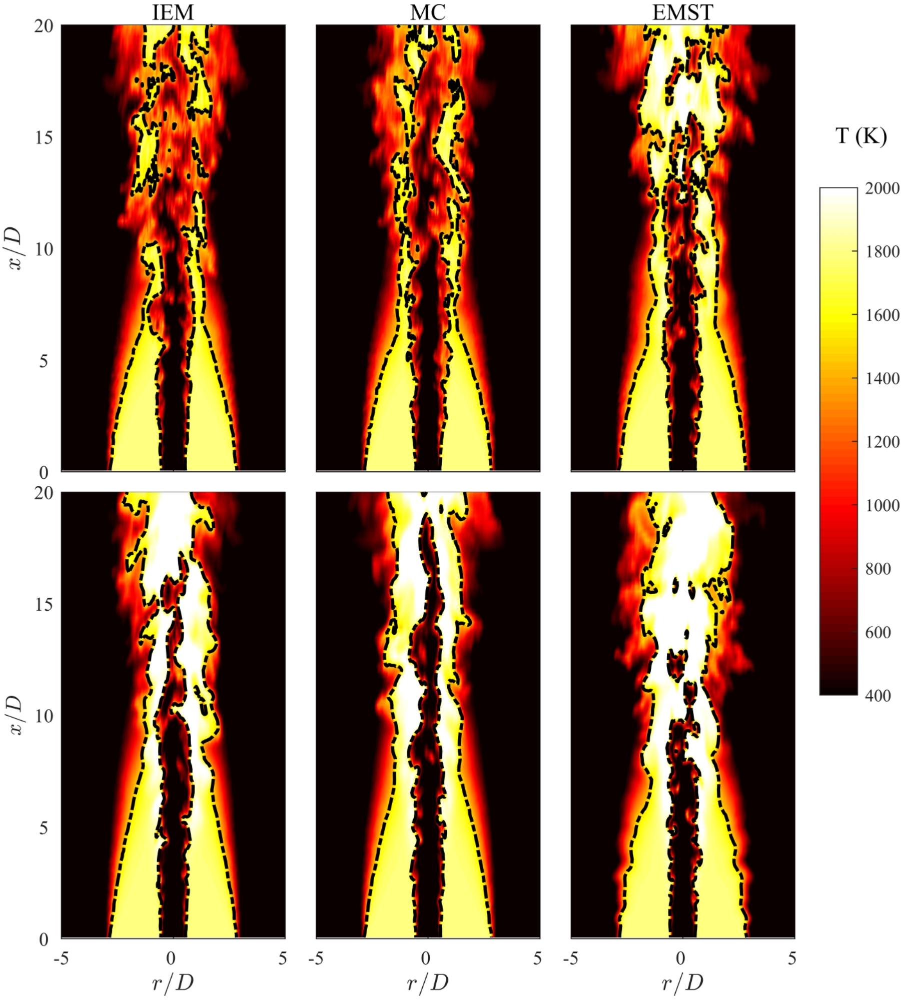

FIG. 1. The contour plots of the predicted instantaneous flame temperature in flame F3 using the IEM model, MC model, and EMST model with different mixing timescale model constants (the first row: $C_M = 2$; the second row: $C_M = 12$).

plots of the instantaneous temperature field. An isoline of $\tilde{T} = 1500$ K is also shown to indicate the flame front. The intersection of the isoline and centerline indicates the instantaneous axial position of the flame tip, and the flame length is defined as the axial distance of the flame tip. As can be observed, the increasing of C_M from 2 to 12 leads to the enhancement of the predicted combustion process, regardless of the micromixing model, i.e., IEM, MC, or EMST being applied. Specifically, when $C_M = 2$, the flame front indicated by $\tilde{T} = 1500$ K is broken with obvious flame holes, and the peak temperature is just slightly higher than the pilot temperature of 1785 K within the axial distance of $x/D = 8$, indicating that the chemical reaction is weak in general. When the model constant C_M is increased to 12, the flame front becomes more continuous with much fewer flame holes, and the highest temperature is close to the adiabatic flame temperature of the unburnt methane-air mixture, i.e., 2200 K. All these illustrate that chemical reaction becomes much stronger by increasing C_M from 2 to 12. Furthermore, for a certain C_M, it is evident that the predictions by the IEM and MC models are similar to each other, and the reaction intensity is weaker than that by the EMST model. For example, when $C_M = 2$, there exist more flame holes simulated by the IEM and MC models

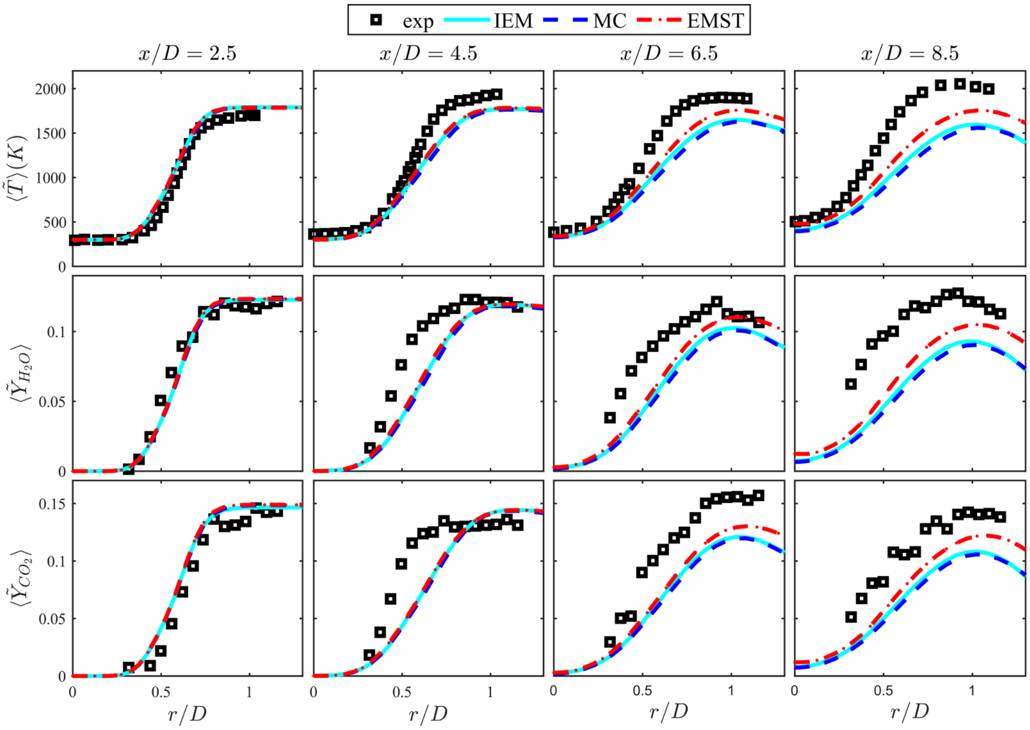

FIG. 2. The radial profiles of the time-averaged mean temperature ($\langle\tilde{T}\rangle$), mean mass fraction of H_2O ($\langle\tilde{Y}_{H_2O}\rangle$), and mean mass fraction of CO_2 ($\langle\tilde{Y}_{CO_2}\rangle$) by the IEM, MC, and EMST models, respectively, using $\Omega_i^{\mathrm{const}}$ with $C_M = 2$.

compared to the EMST model; the former two models even predict an open-tip flame due to a weak chemical reaction. When $C_M = 12$, the flame lengths simulated by the IEM, MC, and EMST models are about $17D$, $19D$, and $11D$, respectively; the shorter flame length predicted by the EMST model again illustrates a stronger and faster combustion process compared to the IEM and MC models.

To investigate the effects of micromixing models on LES/FDF simulations more quantitatively, the radial profiles of the ensemble-averaged mean temperature ($\langle\tilde{T}\rangle$), and mean mass fraction of H_2O and CO_2 ($\langle\tilde{Y}_{H_2O}\rangle$ and $\langle\tilde{Y}_{CO_2}\rangle$), at different axial locations in flame F3 are shown, respectively. When $C_M = 2$, as shown in Fig. 2, simulations with all three mixing formulations underpredict the overall combustion process indicated by the mean temperature, H_2O and CO_2 to a certain extent. Upstream at $x/D = 2.5$, there is almost no difference among the three mixing models since the position is near the inlet. Downstream at $x/D = 6.5$, the peak mean temperature is underpredicted by about 251, 272, and 145 K, with the IEM, MC, and EMST models, respectively. Further downstream at $x/D = 8.5$, the deviation from experimental measurement in terms of the peak mean temperature further increases to 459, 494, and 300 K. It is interesting to note that despite the seemingly drastic difference in model formulation between the IEM and MC models, the predictions by the two models are very similar to each other. Specifically, as is shown above, the maximum difference in mean temperature between the IEM and the MC is only 21 and 35 K at $x/D = 6.5$ and $x/D = 8.5$, respectively. This could be attributed to the fact that both the MC and the IEM models ignore the localness in composition space. By accounting for the localness in composition space, the EMST model predicts a notably higher mean temperature, especially at downstream, resulting in better agreement with the experiment. Nevertheless, the EMST model with $C_M = 2$ still underpredicts the peak mean temperature, as well as the mass fraction of H_2O and CO_2 by about 15%. These findings

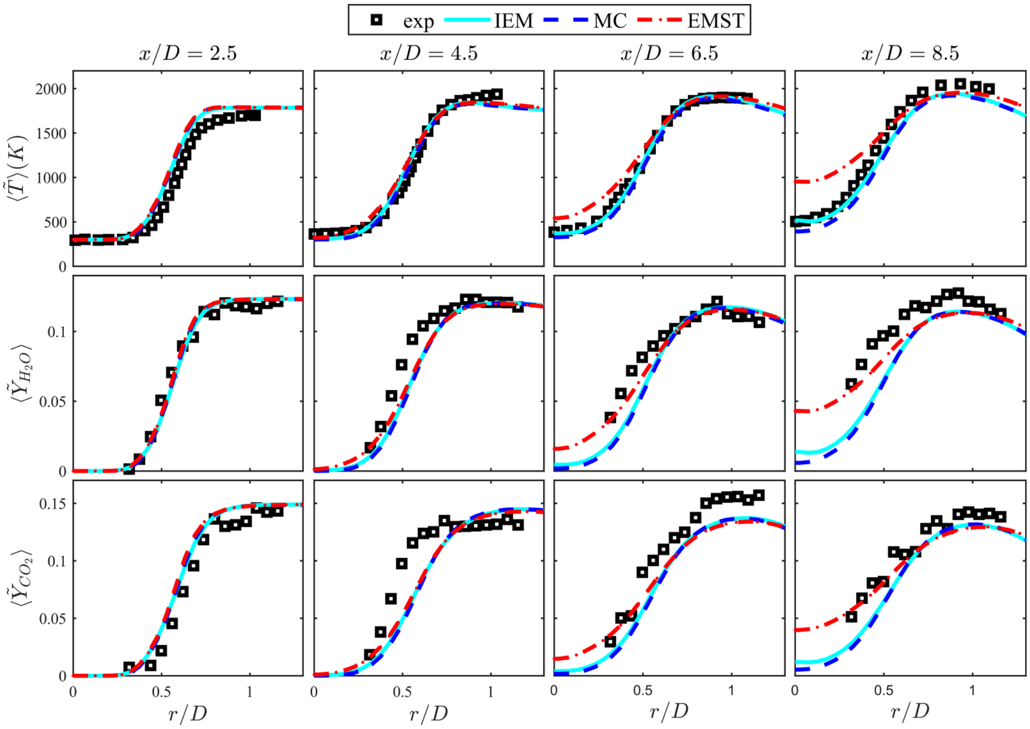

FIG. 3. The radial profiles of the ensemble-averaged mean temperature ($\langle\tilde{T}\rangle$), mean mass fraction of H_2O ($\langle\tilde{Y}_{H_2O}\rangle$), and mean mass fraction of CO_2 ($\langle\tilde{Y}_{CO_2}\rangle$) by the IEM, MC, and EMST models, respectively, using Ω_i^{const} with $C_M = 12$.

illustrate that by applying the constant mechanical-to-scalar mixing timescale model (Ω_i^{const}) with $C_M = 2$, all three micromixing models fail to reproduce the overall combustion process.

To investigate whether the overall combustion process of the target flame can be reproduced by using an optimal global C_M, Fig. 3 presents the results of LES/FDF simulations using the (Ω_i^{const}) model with $C_M = 12$. Compared to the results with $C_M = 2$, the selection of $C_M = 12$ notably improves the prediction of the mean temperature and species when the IEM or MC model is employed for micromixing. For instance, the deviation from the experiment in terms of mean peak temperature is reduced from ~250 to ~12 K at $x/D = 6.5$, and from ~470 to ~120 K at $x/D = 8.5$. The error in peak $\langle\tilde{Y}_{H_2O}\rangle$ reduces from 16% to 3% at $x/D = 6.5$, and from 28% to 10% at $x/D = 8.5$. In general, simulation by the IEM or the MC model adopting the constant mechanical timescale model with $C_M = 12$ provides a reasonable prediction on the mean temperature and mean mass fraction of major species, illustrating that the optimal value of C_M for the IEM and the MC models is around 12. As for EMST model, adopting $C_M = 12$ instead of $C_M = 2$ is capable of better predicting the mean peak temperature; however, the centerline mean temperature downstream gets notably overpredicted. Specifically, the mean temperature of the centerline is overpredicted by 157 K at $x/D = 6.5$ and by 449 K at $x/D = 8.5$. The prediction of the mean mass fraction of the major species, i.e., H_2O and CO_2, on the centerline is also consistently higher than the simulation with $C_M = 2$. These findings illustrate that the EMST model with $C_M = 12$ overpredicts the overall combustion process; therefore, the optimal C_M for EMST is expected to be between 2 and 12.

To further illustrate the difference between the IEM, MC, and EMST models when the constant mechanical timescale model (Ω_i^{const}) with $C_M = 12$ is employed, Fig. 4 shows the PDFs of the progress variable (c) plotted over the sample space variable at two specific positions considered. The sampling particles are extracted from the positions with a range of $0.2D$, e.g., $2.4 < x/D < 2.6$

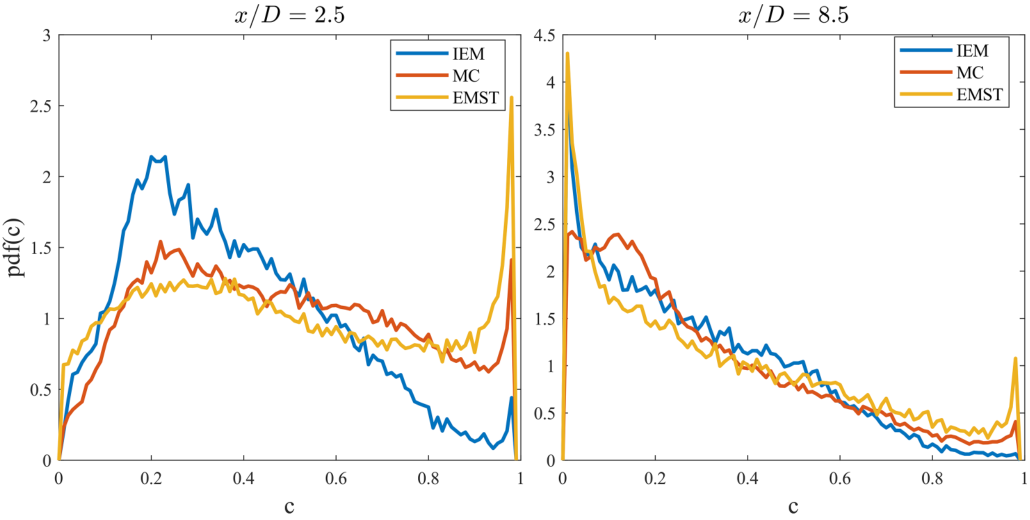

FIG. 4. PDFs of the reaction progress variable at positions $x/D = 2.5$, $r/D = 0.6$ (left) and $x/D = 8.5$, $r/D = 0.5$ (right) using Ω_i^{const} with $C_M = 12$ with the IEM, MC, and EMST models.

for position $x/D = 2.5$, and $0.5 < r/D < 0.7$ for $r/D = 0.6$. Thus, the sampling region consists of a $0.2D \times 0.2D$ annular area. The two selected positions are at $x/D = 2.5$ with $r/D = 0.6$, and $x/D = 8.5$ with $r/D = 0.5$, which locate within the flame-brush region at the corresponding axial location according to Fig. 1. In order to reduce the statistical error, particles are sampled for 800 time steps, resulting in about 3×10^6 samples in total. At $x/D = 2.5$ and $r/D = 0.6$, the PDFs of the progress variable exhibit two peaks near $c = 0.2$ and $c = 1$. The peak near $c = 0.2$ results from the mixing process of particles in the jet and the pilot stream, while the other peak is the result of flame stabilization through the pilot stream, and therefore exhibits a high probability of finding burning particles. It is evident that for the IEM model the peak due to the mixing process is higher, while for the EMST model the peak corresponding to the stabilization process is higher. As for the position at $x/D = 8.5$ and $r/D = 0.5$, the peak near $c = 0.2$ shifts to $c \approx 0$, corresponding to the preheated particles due to the entrainment of cold particles from coflow. Compared to the IEM and MC models, the EMST model predicts a notably higher peak close to $c = 1$, illustrating that more particles are close to the fully burnt state. This implies a faster overall combustion process predicted by the EMST model than that by the IEM or the MC model, consistent with the findings in Fig. 3.

The findings from Figs. 1–4 illustrate that the LES/FDF simulation on the target F3 flame is sensitive to the micromixing model applied, i.e., the EMST model shows different mixing behavior compared with the IEM and MC models. More importantly, the modeling of the mixing timescale is essential to correctly predict the combustion process. For example, the LES/FDF simulation with the constant mechanical timescale model with $C_M = 2$ notably underpredicts the overall combustion process regardless of the micromixing model being applied. Although the IEM and MC models can predict the overall combustion process reasonably well by applying the constant mechanical-to-scalar mixing timescale model (Ω_i^{const}) with an optimal C_M of 12, the optimal value of C_M is case dependent and mixing model dependent. Thus, it could be hard to manually specify an appropriate C_M given a new configuration, which justifies the necessity of developing a more advanced mixing timescale model.

Considering that the IEM and MC models yield similar predictions given the same mixing frequency, the following study employs the MC and MC-DD micromixing model to investigate the effects of mixing timescale models. Note that investigation based on the EMST and the EMST-DD models is certainly valuable; however, one cannot explicitly enforce the variance decay rate of each

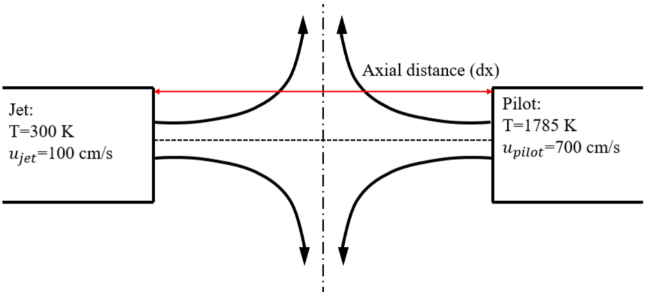

FIG. 5. The schematic plot of laminar reference opposed flame for the reconstruction of Ω_i^f.

individual species, for the reason that the species decay rates depend on the shape of the Euclidean mixing tree in the composition space. In the following, the results predicted by the MC and MC-DD models are presented unless otherwise stated.

B. Effects of mixing timescale models

To investigate the effects of mixing timescale models, LES/FDF simulations are performed using the MC micromixing model with various scalar mixing timescale models, i.e., $\Omega_i^{\mathrm{const}}$ [Eq. (9)], Ω_i^{Dyn} [Eq. (10)], and Ω_i^{Hyb} [Eq. (11)]. To apply Ω_i^{Hyb}, a laminar reference flame needs to be specified. Note that the constant C_M for the $\Omega_i^{\mathrm{const}}$ model is given by the optimal value of 12 in the following investigations. Figure 5 presents the schematic plot of a laminar opposed flame composed of jet and pilot streams, which is chosen as the reference flame to mimic the combustion characteristics of the target flame. As illustrated in Fig. 1, the central jet is mostly surrounded by the pilot stream for the region within the axial distance of $x/D = 8$. Considering that the F3 flame is close to the flamelet regime far from extinction, a moderate bulk strain rate of 700 s^{-1} is applied to the opposed flame. It is worth noting that the prediction by the Ω_i^{Hyb} model exhibits minor sensitivity to the bulk strain rate of the reference flame if the imposed bulk strain rate is far from extinction.

The radial profiles of the mean temperature, species mass fraction of H_2O and CO_2 predicted by LES/FDF simulations with various mixing timescale models are presented in Fig. 6. As can be observed, the simulation with dynamic closure for the mixing timescale (Ω_i^{Dyn}) notably underpredicts the temperature and major product species, e.g., the peak temperature is underpredicted by 361 K at $x/D = 6.5$ and 586 K at $x/D = 8.5$. This implies that the Ω_i^{Dyn} model predicts a much slower combustion process. It is worth noting that the Ω_i^{Dyn} model is a widely applied dynamic closure for the subgrid variance of passive scalars. However, the failure of the Ω_i^{Dyn} model indicates that ignoring the effect of chemical reaction on scalar mixing may result in large error for reactive scalars, i.e., chemical species and progress variable. In comparison, the LES/FDF simulation with the hybrid mixing timescale model (Ω_i^{Hyb}) reasonably well reproduces the distribution of the mean temperature and major species measured by experiment, illustrating that the Ω_i^{Hyb} better models the species mixing frequency by accounting for the reaction-induced scalar gradients. It is worth noting that in general the Ω_i^{Hyb} model has a similar prediction as the $\Omega_i^{\mathrm{const}}$ model with $C_M = 12$, namely, that the former one does not exhibit superior performance in terms of accuracy. For instance, the peak mean temperature at $x/D = 8.5$ is overpredicted by 19 K with Ω_i^{Hyb} and underpredicted by 133 K with $\Omega_i^{\mathrm{const}}$, while the relative error in the peak mean H_2O mass fraction (computed by normalizing the difference in peak $\langle \tilde{Y}_{H_2O} \rangle$ between the simulation and the experiment by the peak value of $\langle \tilde{Y}_{H_2O} \rangle$ in experiment) at $x/D = 8.5$ is 6% with Ω_i^{Hyb} and 10% with $\Omega_i^{\mathrm{const}}$. Nevertheless,

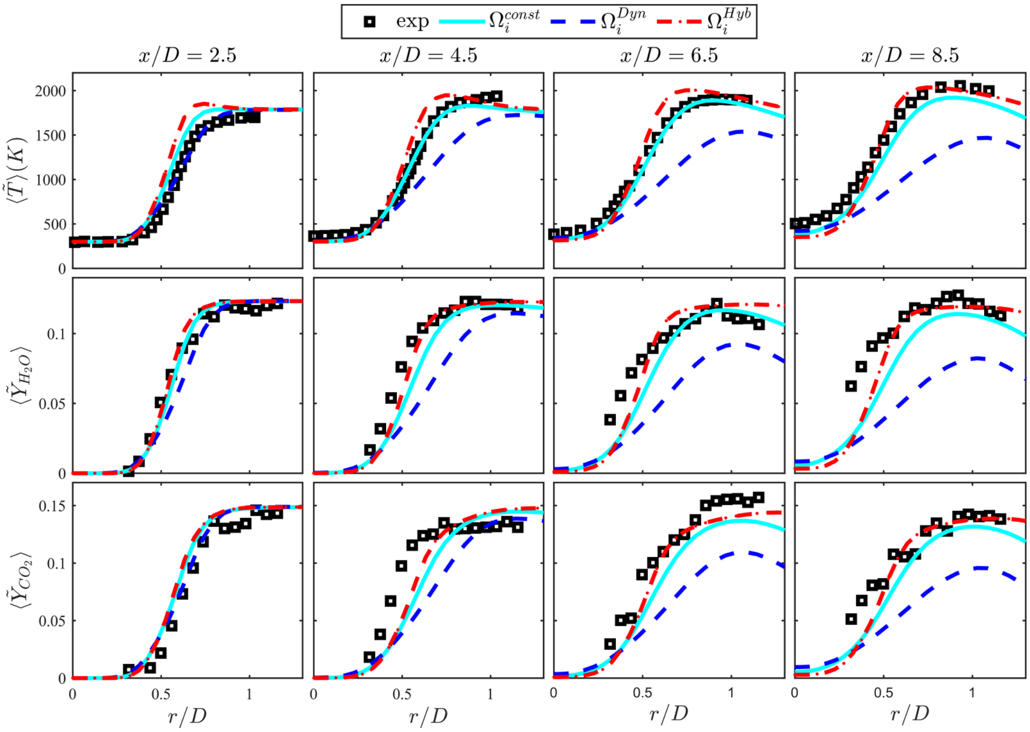

FIG. 6. The radial profiles of the ensemble-averaged mean temperature ($\langle\tilde{T}\rangle$), mean mass fraction of H_2O ($\langle\tilde{Y}_{H_2O}\rangle$), and mean mass fraction of CO_2 ($\langle\tilde{Y}_{CO_2}\rangle$) by different mixing timescale models.

this does not diminish the advantage of the Ω_i^{Hyb} model, since the hybrid mixing timescale model requires no *ad hoc* parameters to be specified manually.

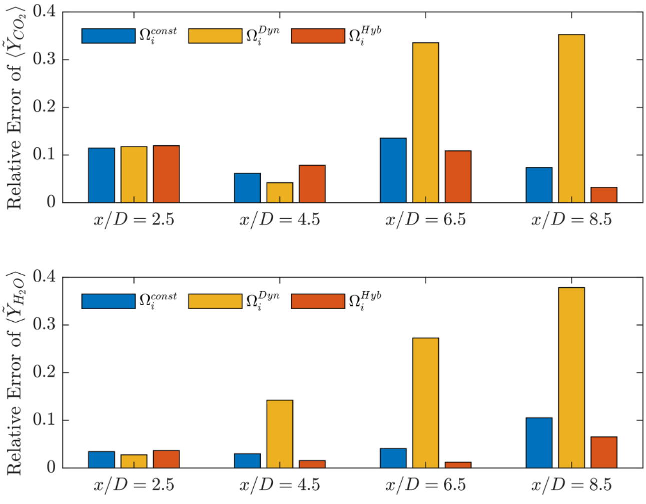

FIG. 7. The relative error on the mean mass fraction $\langle\tilde{Y}_{CO_2}\rangle$ (above) and $\langle\tilde{Y}_{H_2O}\rangle$ (below) with experiment for different mixing timescale models.

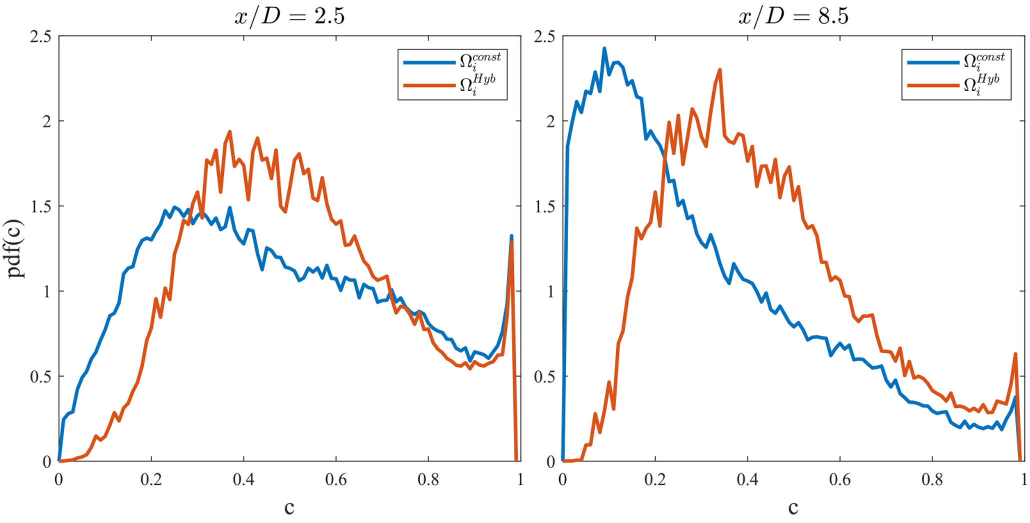

FIG. 8. PDFs of the reaction progress variable at positions $x/D = 2.5$, $r/D = 0.6$ (left), and $x/D = 8.5$, $r/D = 0.5$ (right) with different mixing timescale models.

To further illustrate the performance of different timescale models, Fig. 7 presents the relative error of peak $\langle \tilde{Y}_{\mathrm{CO_2}} \rangle$ and $\langle \tilde{Y}_{\mathrm{H_2O}} \rangle$ at different axial locations, which are computed by normalizing the difference in peak values between the simulation and the experiment by the peak value in experiment. At the upstream of $x/D = 2.5$, all three mixing timescale models yield similar predictions of $\langle \tilde{Y}_{\mathrm{CO_2}} \rangle$ and $\langle \tilde{Y}_{\mathrm{H_2O}} \rangle$. This is because these two quantities are mostly governed by the mixing process between the jet and the pilot in the near-field region. Moving downstream, as the reaction-induced scalar gradient plays a more important role, the error in terms of peak $\langle \tilde{Y}_{\mathrm{CO_2}} \rangle$ and $\langle \tilde{Y}_{\mathrm{H_2O}} \rangle$ at $x/D = 8.5$ is over 30% when the Ω_i^{Dyn} model is employed. The performance of the Ω_i^{Hyb} model is in general similar to that of the $\Omega_i^{\mathrm{const}}$ model with an optimal $C_M = 12$; the former one slightly better predicts the peak $\langle \tilde{Y}_{\mathrm{CO_2}} \rangle$ and $\langle \tilde{Y}_{\mathrm{H_2O}} \rangle$ at $x/D = 6.5$ and $x/D = 8.5$. These findings are consistent with Fig. 6, and again illustrate the advantages of the Ω_i^{Hyb} model, i.e., the model reasonably well reproduces the overall combustion process without the need to tune any model parameter.

The findings above illustrate that Ω_i^{Hyb} and $\Omega_i^{\mathrm{const}}$ with an optimal C_M exhibit similar predictions on the mean quantities. To reveal the difference between these two models, Fig. 8 presents the PDF of the progress variable within the flame brush at $x/D = 2.5$ and $x/D = 8.5$, respectively. As can be observed, the progress variable having the largest probability shifts to a higher value when Ω_i^{Hyb} is employed, implying that the Ω_i^{Hyb} model predicts a faster combustion progress than $\Omega_i^{\mathrm{const}}$. This is consistent with the higher mean temperature and product species predicted by Ω_i^{Hyb} shown in Fig. 6. Given the limited experimental data, it is hard to justify whether the faster combustion process predicted by Ω_i^{Hyb} is closer to reality or not. Additional experiment or DNS data that provide PDF information would serve this purpose, which is the focus of future study.

C. Analysis on reaction-induced subgrid scalar mixing

The success of the Ω_i^{Hyb} model, as well as the failure of the Ω_i^{Dyn} model presented in the previous section, implies that reaction-induced scalar gradient plays an important role in determining the species mixing frequency. Therefore, further analysis of reaction-induced scalar mixing is presented in this section.

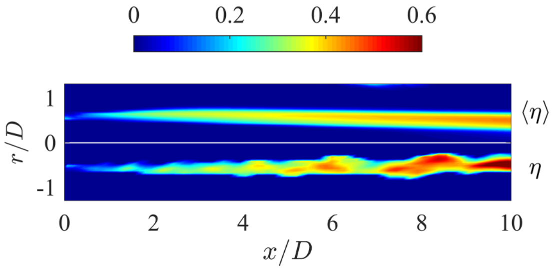

FIG. 9. The spatial distribution of ensembled-averaged and instantaneous segregation factors.

Figure 9 shows the spatial distribution of the segregation factor η; by its construction, η approaches 1 when local Da $\gg 1$, and approaches 0 when Da $\ll 1$. Both the instantaneous segregation factor η and the ensemble-averaged segregation factor $\langle\eta\rangle$ are plotted for completeness. As can be observed, η is close to zero in most regions, and only deviates from zero in the flame brush. Specifically, the maximum η is 0.5 at $x/D = 2.5$, and the maximum η increases to 0.54 at $x/D = 8.5$. The increase of η with the axial distance is as expected considering that the turbulence frequency reduces as the flow goes downstream, resulting in an increase of the local Da in the flame-brush region. Note that further downstream in the post-flame zone, as the combustion process approaches the end, η approaches zero again. The spatial distribution of ensemble-averaged $\langle\eta\rangle$ also shows that the reaction-induced mixing plays an important role in the reaction zone, consistent with the conclusion based on the instantaneous η.

To quantify the relative importance of the reaction-induced mixing in comparison with the turbulence-induced mixing for flame F3, Fig. 10 presents the axial evolution of the ensemble average ratio of the hybrid mixing frequency of the progress variable over the turbulence-induced mixing frequency $\langle\langle\Omega_c^{\mathrm{Hyb}}\rangle/\langle\Omega^t\rangle|x\rangle$. Specifically, $\langle\Omega_{\mathrm{c}}^{\mathrm{Hyb}}\rangle$ and $\langle\Omega^t\rangle$ are firstly computed via an ensemble-averaging operation which involves averaging over the circumferential direction and time, then the average of $\langle\Omega_c^{\mathrm{Hyb}}\rangle/\langle\Omega^t\rangle$ over the computational cells within the main flame zone is computed at every axial location to obtain $\langle\langle\Omega_c^{\mathrm{Hyb}}\rangle/\langle\Omega^t\rangle\ |x\rangle$. The main flame zone is defined as $r/D \leqslant 2$ where the mixing and combustion of the central jet mixture mostly occur. As can be observed,

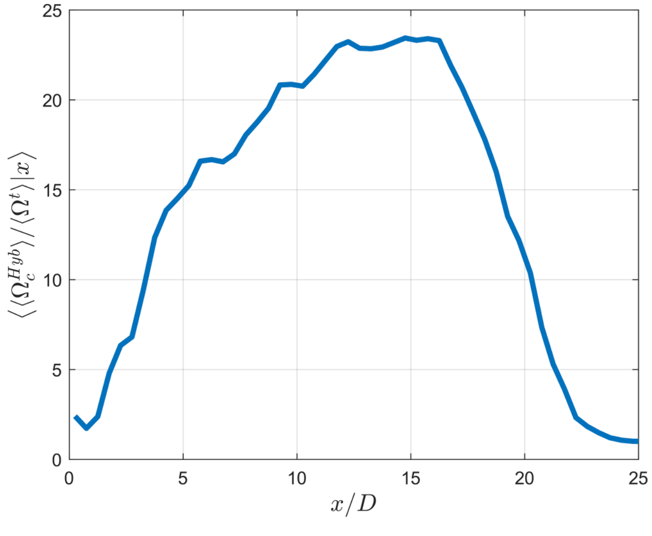

FIG. 10. Axial evolution of the ensemble-averaged ratio $\langle\langle\Omega_c^{\mathrm{Hyb}}\rangle/\langle\Omega^t\rangle|x\rangle$.

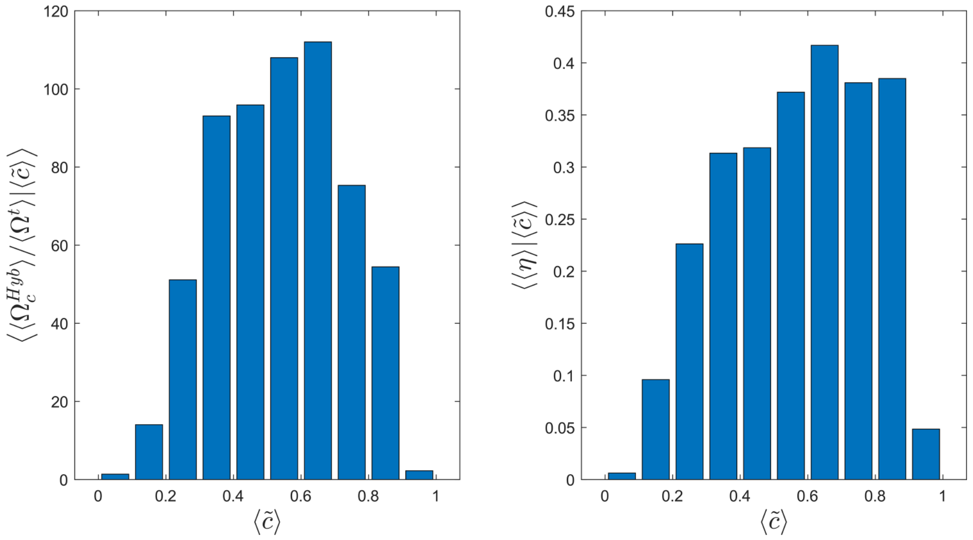

FIG. 11. Conditional averaged mixing frequency ratio on mean progress variable $\langle\langle\Omega_c^{\mathrm{Hyb}}\rangle/\langle\Omega^t\rangle|\langle\tilde{c}\rangle\rangle$ (left) and conditional averaged segregation factor $\langle\langle\eta\rangle|\langle\tilde{c}\rangle\rangle$ (right).

the ratio of $\langle\Omega_c^{\mathrm{Hyb}}\rangle$ over $\langle\Omega^t\rangle$ is close to unity in the near-field region of $x/D \leqslant 1$, indicating that turbulence-induced mixing is the dominating factor for scalar mixing in the near-field region. This is as expected since the large velocity gradient at the inlet results in strong turbulence strain which dominates the formation of scalar gradients. The slight deviation from unity can be attributed to the variation of the progress variable, which is 0 in the central jet and 1 in the pilot stream, which appears right at the nozzle exit. The ratio of $\langle\langle\Omega_c^{\mathrm{Hyb}}\rangle/\langle\Omega^t\rangle|x\rangle$ increases quickly with the axial distance as reaction-induced scalar gradients play a more important role, specifically, $\langle\langle\Omega_c^{\mathrm{Hyb}}\rangle/\langle\Omega^t\rangle|x\rangle$ is over 15 at $x/D = 5$ and over 20 at $x/D = 10$. Moving further downstream to the post-flame region, $\langle\langle\Omega_c^{\mathrm{Hyb}}\rangle/\langle\Omega^t\rangle|x\rangle$ decreases with the axial distance and approaches unity again after $x/D = 22$ where chemical reaction becomes less intensive and the scalar gradient is again dominated by turbulent strain.

To better illustrate the effect of reaction-induced mixing frequency on the whole combustion process, the ratio of $\langle\Omega_c^{\mathrm{Hyb}}\rangle$ over $\langle\Omega^t\rangle$ as well as the segregation factor ($\langle\eta\rangle$) is conditionally averaged on the mean progress variable, i.e., $\langle\langle\Omega_c^{\mathrm{Hyb}}\rangle/\langle\Omega^t\rangle|\langle\tilde{c}\rangle\rangle$ and $\langle\langle\eta\rangle|\langle\tilde{c}\rangle\rangle$ where $\langle\tilde{c}\rangle$ is the mean progress variable indicating the overall combustion process. $\langle\Omega_c^{\mathrm{Hyb}}\rangle$, $\langle\Omega^t\rangle$, and $\langle\eta\rangle$ are firstly computed via an ensemble-averaging operation which involves averaging over the circumferential direction and time. Then, the average of $\langle\Omega_c^{\mathrm{Hyb}}\rangle/\langle\Omega^t\rangle$ and $\langle\eta\rangle$ over the computational cells within the main flame zone is computed at each bin of $\langle\tilde{c}\rangle$ (ten bins in total) to formulate the conditional mean quantities. As shown in Fig. 11, for the unburnt mixture indicated by $\langle\tilde{c}\rangle < 0.1$, $\langle\langle\Omega_c^{\mathrm{Hyb}}\rangle/\langle\Omega^t\rangle|\langle\tilde{c}\rangle\rangle$ is around unity and $\langle\langle\eta\rangle|\langle\tilde{c}\rangle\rangle$ is close to zero, indicating that turbulent mixing is the dominating factor for scalar mixing. In the preheat zone indicated by $0.1 < \langle\tilde{c}\rangle < 0.5$, both $\langle\langle\Omega_c^{\mathrm{Hyb}}\rangle/\langle\Omega^t\rangle|\langle\tilde{c}\rangle\rangle$ and $\langle\langle\eta\rangle|\langle\tilde{c}\rangle\rangle$ consistently increase with $\langle\tilde{c}\rangle$, as a result of the increasingly important role of reaction-induced scalar mixing, i.e., $\langle\langle\Omega_c^{\mathrm{Hyb}}\rangle/\langle\Omega^t\rangle|\langle\tilde{c}\rangle\rangle$ increases from about 1 at $\langle\tilde{c}\rangle = 0.1$ to around 95 at $\langle\tilde{c}\rangle = 0.5$, and $\langle\langle\eta\rangle|\langle\tilde{c}\rangle\rangle$ increases from lower than 0.1 at $\langle\tilde{c}\rangle = 0.1$ to 0.4 at $\langle\tilde{c}\rangle = 0.5$. In the reaction zone indicated by $0.5 < \langle\tilde{c}\rangle < 0.9$, $\langle\langle\Omega_c^{\mathrm{Hyb}}\rangle/\langle\Omega^t\rangle|\langle\tilde{c}\rangle\rangle$ reaches its maximum of over 110, while $\langle\langle\eta\rangle|\langle\tilde{c}\rangle\rangle$ also reaches its peak magnitude of over 0.41. Finally, in the post-flame zone indicated by $\langle\tilde{c}\rangle > 0.9$, $\langle\langle\Omega_c^{\mathrm{Hyb}}\rangle/\langle\Omega^t\rangle|\langle\tilde{c}\rangle\rangle$ and $\langle\langle\eta\rangle|\langle\tilde{c}\rangle\rangle$ recover to unity and zero, respectively, indicating that scalar mixing is again dominated by turbulence. The findings from both Figs. 10 and 11 illustrate the importance

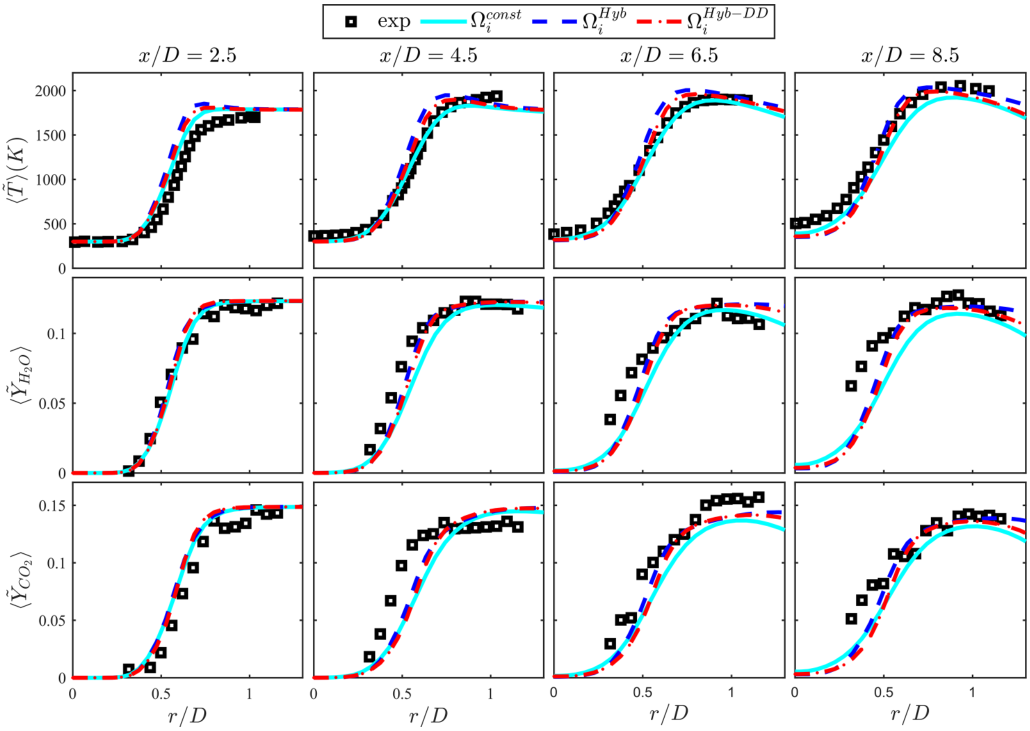

FIG. 12. The radial profiles of the ensemble-averaged mean temperature ($\langle\tilde{T}\rangle$), mean mass fraction of H_2O ($\langle\tilde{Y}_{H_2O}\rangle$), and mean mass fraction of CO_2 ($\langle\tilde{Y}_{CO_2}\rangle$) by different mixing timescale models.

of reaction-induced mixing in the flame considered, and therefore provide an explanation for the good performance of the Ω_i^{Hyb} model which accounts for the effect of chemical reaction on scalar mixing.

D. Effect of subgrid scalar differential mixing

To investigate the potential benefit of incorporating the reaction-induced differential mixing timescale, LES/FDF simulation has been performed using the MC-DD micromixing model with the mixing timescale of each species modeled by the hybrid-DD model, i.e., $\Omega_i^{\mathrm{Hyb-DD}}$. Figure 12 presents the radial profiles of the mean temperature and species mass fraction; the results predicted by the Ω_i^{Hyb} model and the $\Omega_i^{\mathrm{const}}$ model with an optimal $C_M = 12$ are also shown for comparison. As shown, the $\Omega_i^{\mathrm{Hyb-DD}}$ model slightly better predicts the mean temperature than the Ω_i^{Hyb} model, but the improvement is minor. In general, these three mixing timescale models yield similar accuracy in terms of the prediction for mean temperature and major species, implying that differential mixing has a minor impact on the overall combustion process for the flame considered.

To further investigate the effect of incorporating differential mixing on th flame structure, the conditional mean and PDF of the CO mass fraction in the progress variable space predicted by the $\Omega_i^{\mathrm{Hyb-DD}}$ and Ω_i^{Hyb} models are presented in Fig. 13. Three regions located at $x/D = 2.5,\ 6.5$, and 8.5 and within $0 < r/D < 1$ are chosen as sampling regions, and computational particles in these regions are sampled for statistics. As can be observed, for a certain progress variable, $\Omega_i^{\mathrm{Hyb-DD}}$ predicts a notably wider conditional PDF than Ω_i^{Hyb}, indicating that the former one exhibits a larger conditional fluctuation. This is as expected considering that accounting for the differential mixing among species would result in more abundant thermochemical states. In

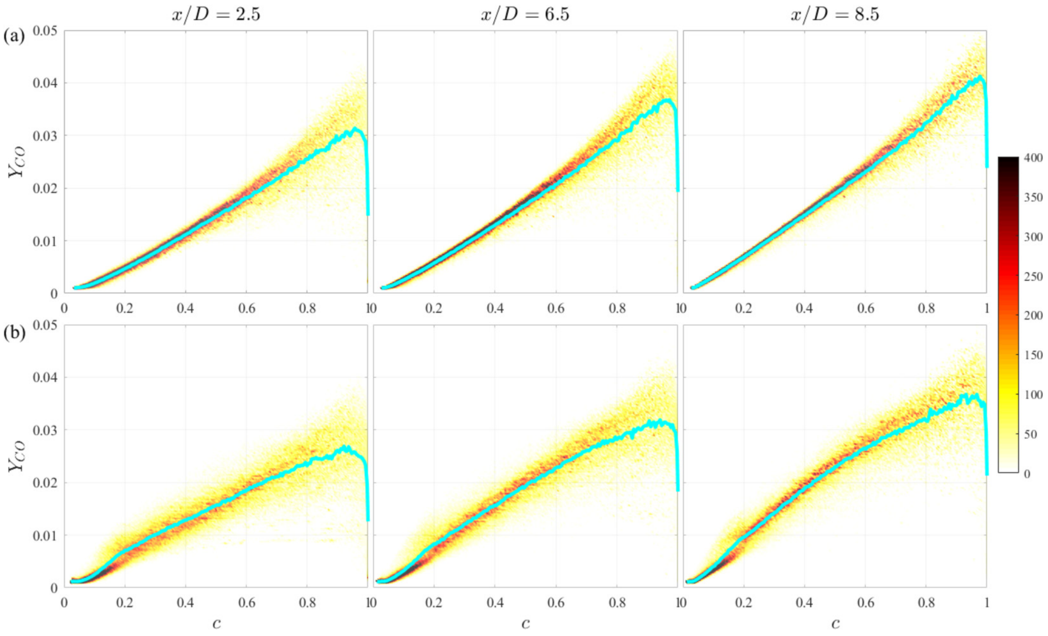

FIG. 13. Conditional mean and conditional PDFs of CO mass fraction in progress variable space at 2.5*D*, 6.5*D*, and 8.5*D* of the F3 flame with the (a) hybrid model and the (b) hybrid-DD model.

addition, the peak magnitude of the conditional mean CO mass fraction $\langle Y_{\mathrm{CO}}|c\rangle$ is found to increase with the axial distance for both mixing timescale models. This could be attributed to the reduction of local strain, as found in the laminar opposed flame where peak Y_{CO} increases with the decrease of the bulk strain rate. Moreover, compared to the Ω_i^{Hyb} model, the $\Omega_i^{\mathrm{Hyb-DD}}$ model predicts a higher conditional mean $\langle Y_{\mathrm{CO}}|c\rangle$ in the preheat zone indicated by $0.1 < c < 0.5$. For example, at the location of $x/D = 8.5$, $\langle Y_{\mathrm{CO}}|c\rangle$ for $c = 0.4$ is around 0.02 when $\Omega_i^{\mathrm{Hyb-DD}}$ is applied and 0.015 when Ω_i^{Hyb} is applied. To justify whether the higher $\langle Y_{\mathrm{CO}}|c\rangle$ in the preheat zone predicted by $\Omega_i^{\mathrm{Hyb-DD}}$ is more accurate or not, additional experiment or DNS data is needed, which is the focus of a future study.

Figure 14 presents the mixing frequencies of representative species over that of the progress variable predicted by the $\Omega_i^{\mathrm{Hyb-DD}}$ model. Species $\mathrm{CO_2}$, $\mathrm{H_2O}$, OH, and CO are chosen for

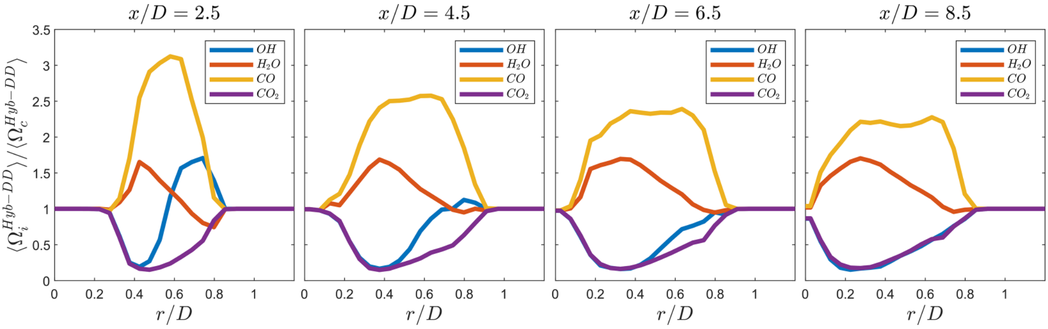

FIG. 14. The ratio of mixing frequencies of representative species ($\langle\Omega_i^{\mathrm{Hyb-DD}}\rangle$) over the mixing frequency of progress variable ($\langle\Omega_c^{\mathrm{Hyb-DD}}\rangle$) at different axial positions.

analysis; the former two are representative major species, while the latter two are representative intermediate species. As can be observed in Fig. 14, in the flame-brush region at $x/D = 2.5$, $\langle\Omega_{\mathrm{CO}}^{\mathrm{Hyb-DD}}\rangle/\langle\Omega_c^{\mathrm{Hyb-DD}}\rangle$ is mostly larger than unity, while $\langle\Omega_{\mathrm{CO_2}}^{\mathrm{Hyb-DD}}\rangle/\langle\Omega_c^{\mathrm{Hyb-DD}}\rangle$ is mostly smaller than unity, and $\langle\Omega_{\mathrm{H_2O}}^{\mathrm{Hyb-DD}}\rangle/\langle\Omega_c^{\mathrm{Hyb-DD}}\rangle$ and $\langle\Omega_{\mathrm{OH}}^{\mathrm{Hyb-DD}}\rangle/\langle\Omega_c^{\mathrm{Hyb-DD}}\rangle$ could be either larger or smaller than unity depending on the radial location. In the flame-brush region at $x/D = 8.5$, $\langle\Omega_{\mathrm{H_2O}}\rangle/\langle\Omega_c\rangle$ and $\langle\Omega_{\mathrm{CO}}\rangle/\langle\Omega_c\rangle$ are mostly larger than unity, while $\langle\Omega_{\mathrm{CO_2}}\rangle/\langle\Omega_c\rangle$ and $\langle\Omega_{\mathrm{OH}}\rangle/\langle\Omega_c\rangle$ are mostly smaller than unity. The larger than unity $\langle\Omega_{\mathrm{CO}}\rangle/\langle\Omega_c\rangle$ indicates that CO exhibits stronger mixing than the progress variable in the flame-brush region; this may explain the higher $\langle Y_{\mathrm{CO}}|c\rangle$ in the preheat zone predicted by the $\Omega_i^{\mathrm{Hyb-DD}}$ model than by the Ω_i^{Hyb} model. Nevertheless, the hybrid-DD model exhibits the overall similar performance as the hybrid model for the flame F3 studied in this work. A turbulent hydrogen flame where differential diffusion is known to play a more important role could be a better option for evaluating the performance of the hybrid-DD model, which is the focus of our future work.

IV. CONCLUSIONS

In this work, LES/FDF simulation is applied to the turbulent premixed methane-air flame F3 to investigate the effect of incorporating the reaction-induced subgrid scalar mixing on a LES/FDF simulation of turbulent premixed flames. Three widely used micromixing models (IEM, MC, and EMST) are tested in the first place to investigate the effects of mixing formulation on flame characteristics. The predictions by the classic constant mechanical-to-scalar mixing timescale model ($\Omega_i^{\mathrm{const}}$) with various model constants (i.e., $C_M = 2$ and 12) illustrate that the LES/FDF simulation is sensitive to the mixing timescale model constant C_M. It is found that the LES/FDF simulation using $\Omega_i^{\mathrm{const}}$ with $C_M = 2$ notably underpredicts the overall combustion process regardless of the micromixing model (IEM, MC, or EMST) being applied, illustrating that the mixing timescale model is a key component to correctly predicting the combustion process. The failure of the dynamic closure for passive scalar (Ω_i^{Dyn}) implies that ignoring the effect of chemical reaction on scalar mixing may result in large error for reactive scalars. By accounting for the reaction-induced scalar gradients, the hybrid mixing timescale model (Ω_i^{Hyb}) reasonably well reproduces the distribution of the mean temperature and major species.

The effect of reaction-induced mixing on the whole combustion process is further investigated. It is found that for the unburnt mixture, $\langle\langle\Omega_c^{\mathrm{Hyb}}\rangle/\langle\Omega^t\rangle|\langle\tilde{c}\rangle\rangle$ is around unity and $\langle\langle\eta\rangle|\langle\tilde{c}\rangle\rangle$ is close to zero, indicating that turbulent mixing is the dominant factor for scalar mixing. In the preheat zone, both $\langle\langle\Omega_c^{\mathrm{Hyb}}\rangle/\langle\Omega^t\rangle|\langle\tilde{c}\rangle\rangle$ and $\langle\langle\eta\rangle|\langle\tilde{c}\rangle\rangle$ consistently increase with $\langle\tilde{c}\rangle$, as a result of the increasingly important role of reaction-induced scalar mixing. In the reaction zone, both $\langle\langle\Omega_c^{\mathrm{Hyb}}\rangle/\langle\Omega^t\rangle|\langle\tilde{c}\rangle\rangle$ and $\langle\langle\eta\rangle|\langle\tilde{c}\rangle\rangle$ reach their peak magnitude. Finally, in the post-flame zone, $\langle\langle\Omega_c^{\mathrm{Hyb}}\rangle/\langle\Omega^t\rangle|\langle\tilde{c}\rangle\rangle$ and $\langle\langle\Omega_c^{\mathrm{Hyb}}\rangle/\langle\Omega^t\rangle|\langle\tilde{c}\rangle\rangle$ recover to unity and zero, respectively, indicating that scalar mixing is again dominated by turbulence. These findings illustrate that reaction-induced subgrid mixing is of great importance especially in the reaction zone, and thus provide explanations for the accurate prediction by the Ω_i^{Hyb} model.

A new mixing timescale model, hybrid-DD ($\Omega_i^{\mathrm{Hyb-DD}}$), is proposed, which accounts for the reaction-induced differential mixing among species. The LES/FDF simulation with $\Omega_i^{\mathrm{Hyb-DD}}$ yields a reasonable prediction for the mean temperature and mass fraction of major species. The difference between $\Omega_i^{\mathrm{Hyb-DD}}$ and Ω_i^{Hyb} in terms of the mean temperature and major species field is in general minor. Further investigation shows that the former one, i.e., $\Omega_i^{\mathrm{Hyb-DD}}$ predicts a higher conditional mean CO mass fraction in the preheat zone. In addition, the predicted scalar mixing frequency by $\Omega_i^{\mathrm{Hyb-DD}}$ is found to exhibit large differences among species, resulting in more abundant thermochemical states than Ω_i^{Hyb}. However, to justify whether the prediction by $\Omega_i^{\mathrm{Hyb-DD}}$ is more accurate or not, additional experiment or DNS data is needed, which is the focus of a future study. To

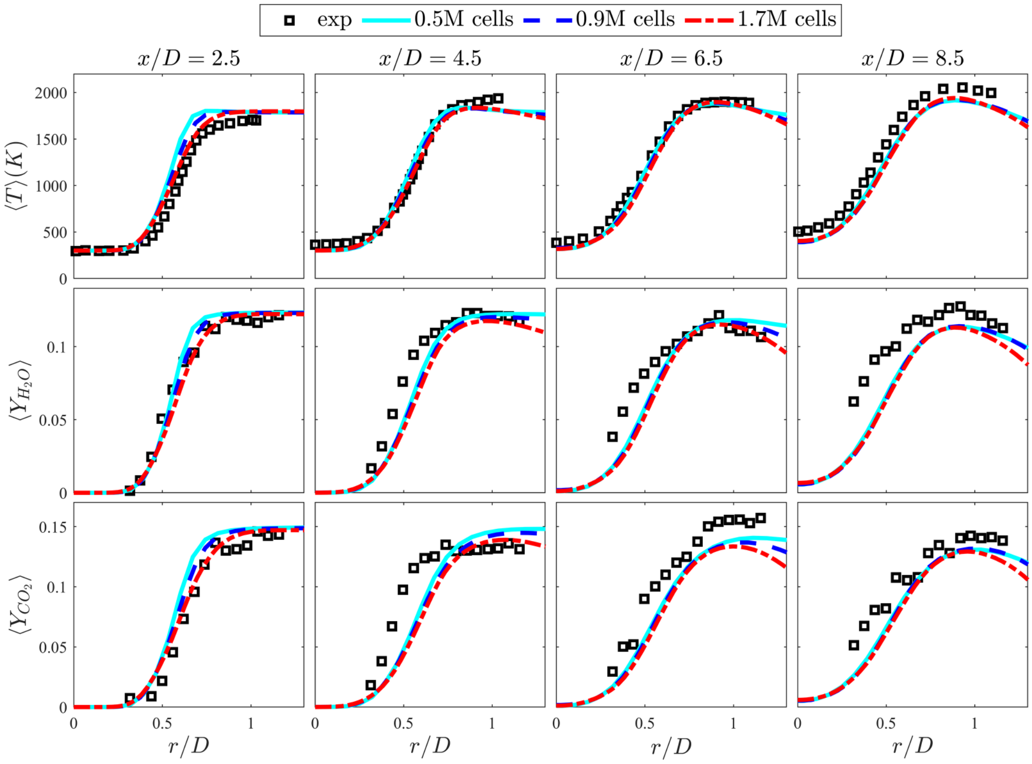

FIG. 15. Radial profiles of the ensemble averaged mean temperature and the mass fraction of H_2O and CO_2 predicted using the three different grids of $0.5M$, $0.9M$, and $1.7M$ cells, respectively, with $C_M = 12$.

summarize, the proposed hybrid-DD model yields a reasonable prediction of the overall combustion process of the flame F3 and requires no *ad hoc* parameters to be specified manually. In addition, all the components of the hybrid-DD model are readily available in the transported FDF method, making it a promising candidate to be employed in LES/FDF simulations of turbulent premixed flames.

ACKNOWLEDGMENTS

This work was supported by the National Natural Science Foundation of China (Grants No. 52025062 and No. 52106166). The authors also acknowledge High-Performance Computing Centre in Tsinghua University for providing computational resources.

APPENDIX

A grid sensitivity study has been performed. The number of cells is $0.5M$, $0.9M$ (baseline), and $1.7M$, respectively. Compared to the baseline grid of $0.9M$ cells, the grid of $0.5M$ cells is ∼1.5× coarser, while the grid of $1.7M$ cells is ∼1.5× finer in the main flame zone. Figure 15 presents the radial profiles of the mean temperature and major species predicted using the three different grids with $C_M = 12$. Compared to the baseline grid, the coarser grid slightly overpredicts the peak temperature, H_2O and CO_2 upstream at $x/D = 2.5$, while the finer grid slightly underpredicts the peak temperature, H_2O and CO_2 downstream. This implies that the optimal C_M for the coarser grid would be slightly smaller than 12, while the optimal C_M for the finer grid would be slightly larger than 12. Nevertheless, the three grids with $C_M = 12$ yield a similar prediction of the mean

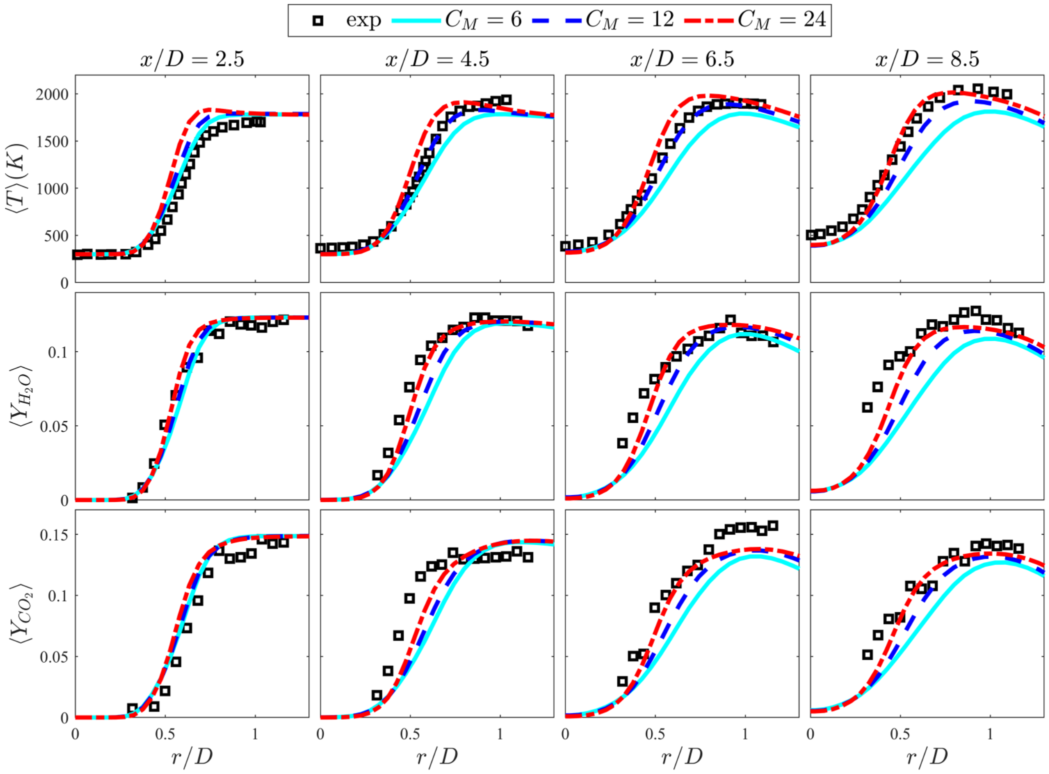

FIG. 16. Radial profiles of the ensemble averaged mean temperature and the mass fraction of H_2O and CO_2 predicted with $C_M = 6$, 12, and 24, respectively.

temperature and major species in general, indicating that the optimal C_M exhibits a minor sensitivity to the grid resolution for the three grids tested.

Additional simulations with $C_M = 6$ and 24 have been performed to illustrate the sensitivity of the simulation results to this parameter. Figure 16 presents the radial profiles of the mean temperature and major species predicted using the three different C_M values. As can be observed, at the four selected locations, the simulation with $C_M = 6$ underpredicts the mean temperature and the mass fraction of H_2O and CO_2, especially for $x/D \geqslant 4.5$, while the simulation with $C_M = 24$ overpredicts the mean temperature and the major species, especially for $x/D = 4.5$ and 6.5. This is as expected given that a higher C_M leads to a larger mixing frequency, which enhances the micromixing and thus the combustion process. The simulation with $C_M = 12$ yields the best agreement with experiment in terms of the mean temperature and the major species. Thus, 12 is the optimal C_M value in a sense that it best reproduces the overall combustion process.

---

[1] S. B. Pope, PDF methods for turbulent reactive flows, Prog. Energy Combust. Sci. **11**, 119 (1985).

[2] D. C. Haworth, Progress in probability density function methods for turbulent reacting flows, Prog. Energy Combust. Sci. **36**, 168 (2010).

[3] P. Givi, Filtered density function for subgrid scale modeling of turbulent combustion, AIAA J. **44**, 16 (2006).

[4] V. Raman and H. Pitsch, A consistent LES/filtered-density function formulation for the simulation of turbulent flames with detailed chemistry, Proc. Combust. Inst. **31**, 1711 (2007).

[5] S. Sammak, Z. Ren, and P. Givi, Modern developments in filtered density function, in *Modeling and Simulation of Turbulent Mixing and Reaction* (Springer, Singapore, 2020), pp. 181–200.

[6] H. Zhou, Z. Ren, D. H. Rowinski, and S. B. Pope, Filtered density function simulations of a near-limit turbulent lean premixed flame, J. Propuls. Power **36**, 381 (2020).

[7] Y. Yin, T. Yang, H. Zhou, and Z. Ren, Assessment of finite-rate chemistry effects in a turbulent dilute ethanol spray flame, J. Propuls. Power **38**, 607 (2022).

[8] Q. Tang, J. Xu, and S. B. Pope, Probability density function calculations of local extinction and no production in piloted-jet turbulent methane/air flames, Proc. Combust. Inst. **28**, 133 (2000).

[9] J. Xu and S. B. Pope, PDF calculations of turbulent nonpremixed flames with local extinction, Combust. Flame **123**, 281 (2000).

[10] M. Muradoglu, K. Liu, and S. B. Pope, PDF modeling of a bluff-body stabilized turbulent flame, Combust. Flame **132**, 115 (2003).

[11] Z. Ren and S. B. Pope, An investigation of the performance of turbulent mixing models, Combust. Flame **136**, 208 (2004).

[12] H. Wang and Y. Chen, PDF modelling of turbulent non-premixed combustion with detailed chemistry, Chem. Eng. Sci. **59**, 3477 (2004).

[13] H. Wang and S. B. Pope, Large eddy simulation/probability density function modeling of a turbulent $CH_4/H_2/N_2$ jet flame, Proc. Combust. Inst. **33**, 1319 (2011).

[14] Y. Yang, H. Wang, S. B. Pope, and J. H. Chen, Large-eddy simulation/probability density function modeling of a non-premixed Co/H_2 temporally evolving jet flame, Proc. Combust. Inst. **34**, 1241 (2013).

[15] X. Y. Zhao, D. C. Haworth, T. Ren, and M. F. Modest, A transported probability density function/photon Monte Carlo method for high-temperature oxynatural gas combustion with spectral gas and wall radiation, Combust. Theory Model. **17**, 354 (2013).

[16] H. Wang and K. Kim, Effect of molecular transport on PDF modeling of turbulent non-premixed flames, Proc. Combust. Inst. **35**, 1137 (2015).

[17] W. Han, V. Raman, and Z. Chen, LES/PDF modeling of autoignition in a lifted turbulent flame: Analysis of flame sensitivity to differential diffusion and scalar mixing time-scale, Combust. Flame **171**, 69 (2016).

[18] J. Wei, X. Su, H. Zhou, E. Hawkes, and Z. Ren, Assessment of *critical species* for differential mixing in transported PDF simulations of a non-premixed ethylene DNS flame, Combust. Flame **244**, 112240 (2022).

[19] J. Wei, X. Su, X. Wang, H. Zhou, E. R. Hawkes, and Z. Ren, A mixing timescale model for differential mixing in transported probability density function simulations of turbulent non-premixed flames, Phys. Fluids **34**, 67122 (2022).

[20] J. Villermaux and J.-C. Devillon, Représentation de la redistribution des domaines de ségrégation dans un fluide par un modéle d'interaction phénoménologique, in *Proceedings of the Second International Symposium on Chemical Reaction Engineering* (Elsevier, Amsterdam, 1972), pp. 1–13.

[21] C. Dopazo and E. E. O'Brien, An approach to the autoignition of a turbulent mixture, Acta Astronaut. **1**, 1239 (1974).

[22] R. L. Curl, Dispersed phase mixing: I. Theory and effects in simple reactors, AIChE J. **9**, 175 (1963).

[23] J. Janicka, W. Kolbe, and W. Kollmann, Closure of the transport equation for the probability density function of turbulent scalar fields, J. Non-Equilib. Thermodyn. **4**, 47 (1979).

[24] S. Subramaniam and S. B. Pope, A mixing model for turbulent reactive flows based on Euclidean minimum spanning trees, Combust. Flame **115**, 487 (1998).

[25] A. Y. Klimenko and S. B. Pope, The modeling of turbulent reactive flows based on multiple mapping conditioning, Phys. Fluids **15**, 1907 (2003).

[26] A. Varna, M. J. Cleary, and E. R. Hawkes, A multiple mapping conditioning mixing model with a mixture-fraction like reference variable. Part 1: Model derivation and ideal flow test cases, Combust. Flame **181**, 342 (2017).

[27] S. B. Pope, A model for turbulent mixing based on shadow-position conditioning, Phys. Fluids **25**, 110803 (2013).

[28] X. Y. Zhao, A. Bhagatwala, J. H. Chen, D. C. Haworth, and S. B. Pope, An *a priori* DNS study of the shadow-position mixing model, Combust. Flame **165**, 223 (2016).

[29] M. Kuron, E. R. Hawkes, Z. Ren, J. C. K. Tang, H. Zhou, J. H. Chen, and T. Lu, Performance of transported PDF mixing models in a turbulent premixed flame, Proc. Combust. Inst. **36**, 1987 (2017).

[30] S. B. Pope, Small scales, many species and the manifold challenges of turbulent combustion, Proc. Combust. Inst. **34**, 1 (2013).

[31] K. N. C. Bray, Turbulent flows with premixed reactants, *Turbulent Reacting Flows*, Topics in Applied Physics Vol. 44 (Springer, Berlin, Heidelberg, 1980), pp. 115–183.

[32] N. Swaminathan and K. N. C. Bray, Effect of dilatation on scalar dissipation in turbulent premixed flames, Combust. Flame **143**, 549 (2005).

[33] K. Bray, M. Champion, P. A. Libby, and N. Swaminathan, Scalar dissipation and mean reaction rates in premixed turbulent combustion, Combust. Flame **158**, 2017 (2011).

[34] S. B. Pope and M. S. Anand, Flamelet and distributed combustion in premixed turbulent flames, Symp. (Int.) Combust., [Proc.] **20**, 403 (1985).

[35] H. Kolla, J. W. Rogerson, N. Chakraborty, and N. Swaminathan, Scalar dissipation rate modeling and its validation, Combust. Sci. Technol. **181**, 518 (2009).

[36] R. P. Lindstedt, S. A. Louloudi, and E. M. Váos, Joint scalar probability density function modeling of pollutant formation in piloted turbulent jet diffusion flames with comprehensive chemistry, Proc. Combust. Inst. **28**, 149 (2000).

[37] R. P. Lindstedt and E. M. Vaos, Transported PDF modeling of high-Reynolds-number premixed turbulent flames, Combust. Flame **145**, 495 (2006).

[38] M. Stöllinger and S. Heinz, Evaluation of scalar mixing and time scale models in PDF simulations of a turbulent premixed flame, Combust. Flame **157**, 1671 (2010).

[39] M. Kuron, Z. Ren, E. R. Hawkes, H. Zhou, H. Kolla, J. H. Chen, and T. Lu, A mixing timescale model for TPDF simulations of turbulent premixed flames, Combust. Flame **177**, 171 (2017).

[40] A. Mura, V. Robin, and M. Champion, Modeling of scalar dissipation in partially premixed turbulent flames, Combust. Flame **149**, 217 (2007).

[41] R. R. Tirunagari and S. B. Pope, LES/PDF for premixed combustion in the DNS limit, Combust. Theory Model. **20**, 834 (2016).

[42] H. Wang, T. Pant, and P. Zhang, LES/PDF modeling of turbulent premixed flames with locally enhanced mixing by reaction, Flow, Turbul. Combust. **100**, 147 (2018).

[43] E. R. Hawkes, R. Sankaran, J. C. Sutherland, and J. H. Chen, Scalar mixing in direct numerical simulations of temporally evolving plane jet flames with skeletal CO/H_2 kinetics, Proc. Combust. Inst. **31**, 1633 (2007).

[44] E. S. Richardson, R. Sankaran, R. W. Grout, and J. H. Chen, Numerical analysis of reaction-diffusion effects on species mixing rates in turbulent premixed methane-air combustion, Combust. Flame **157**, 506 (2010).

[45] H. Zhou, T. Yang, and Z. Ren, Differential diffusion modeling in LES/FDF simulations of turbulent flames, AIAA J. **57**, 3206 (2019).

[46] H. Zhou, Z. Li, T. Yang, E. R. Hawkes, Z. Ren, H. Wang, and A. Wehrfritz, An evaluation of gas-phase micro-mixing models with differential mixing timescales in transported PDF simulations of sooting flame DNS, Proc. Combust. Inst. **38**, 2731 (2021).

[47] H. Zhou, Z. Ren, M. Kuron, T. Lu, and J. H. Chen, Investigation of reactive scalar mixing in transported PDF simulations of turbulent premixed methane-air bunsen flames, Flow, Turbul. Combust. **103**, 667 (2019).

[48] T. Yang, H. Zhou, and Z. Ren, A particle mass-based implementation for mixing models with differential diffusion, Combust. Flame **214**, 116 (2020).

[49] H. Wang, P. P. Popov, and S. B. Pope, Weak second-order splitting schemes for Lagrangian Monte Carlo particle methods for the composition PDF/FDF transport equations, J. Comput. Phys. **229**, 1852 (2010).

[50] P. P. Popov, H. Wang, and S. B. Pope, Specific volume coupling and convergence properties in hybrid particle/finite volume algorithms for turbulent reactive flows, J. Comput. Phys. **294**, 110 (2015).

[51] S. S. Girimaji and Y. Zhou, Analysis and modeling of subgrid scalar mixing using numerical data, Phys. Fluids **8**, 1224 (1996).

[52] C. D. Pierce and P. Moin, A dynamic model for subgrid-scale variance and dissipation rate of a conserved scalar, Phys. Fluids **10**, 3041 (1998).

[53] T. Yang, Q. Xie, H. Zhou, and Z. Ren, On the modeling of scalar mixing timescale in filtered density function simulation of turbulent premixed flames, Phys. Fluids **32**, 115130 (2020).

[54] Y. C. Chen, N. Peters, G. A. Schneemann, N. Wruck, U. Renz, and M. S. Mansour, The detailed flame structure of highly stretched turbulent premixed methane-air flames, Combust. Flame **107**, 223 (1996).

[55] N. Peters, The turbulent burning velocity for large-scale and small-scale turbulence, J. Fluid Mech. **384**, 107 (1999).

[56] C. D. Pierce, *Progress-Variable Approach for Large-Eddy Simulation of Turbulent Combustion* (Stanford University, Stanford, CA, 2001).

[57] A. W. Vreman, An eddy-viscosity subgrid-scale model for turbulent shear flow: Algebraic theory and applications, Phys. Fluids **16**, 3670 (2004).

[58] H. Pitsch and H. Steiner, Large-eddy simulation of a turbulent piloted methane/air diffusion flame (Sandia flame D), Phys. Fluids **12**, 2541 (2000).

[59] C. J. Sung, C. K. Law, and J. Y. Chen, An augmented reduced mechanism for methane oxidation with comprehensive global parametric validation, Symp. Combust. **27**, 295 (1998).

[60] S. B. Pope, Computationally efficient implementation of combustion chemistry using *in situ* adaptive tabulation, Combust. Theory Model. **1**, 41 (1997).